Effect of trailing edge shape on the separated flow characteristics around an airfoil at low Reynolds number: a numerical study

Thomareis, Nikitas[a)] and Papadakis, George

Department of Aeronautics, Imperial College London, London SW7 2AZ, U.K.

(Dated: 4 November 2016)

Direct Numerical Simulations of the flow field around a NACA 0012 airfoil at Reynolds number $50,000$ and angle of attack 5^o with 3 different trailing edge shapes (straight, blunt and serrated) have been performed. Both time-averaged flow characteristics as well as the most dominant flow structures and their frequencies are investigated using the Dynamic Mode Decomposition method (DMD). It is shown that for the straight trailing edge airfoil, this method can capture the fundamental as well as the subharmonic of the Kelvin-Helmholtz instability that develops naturally in the separating shear layer. The fundamental frequency matches well with relevant data in the literature. The blunt trailing edge results in periodic vortex shedding, with frequency close to the subharmonic of the natural shear layer frequency. The shedding, resulting from a global instability, has an upstream effect and forces the separating shear layer. Due to forcing, the shear layer frequency locks onto the shedding frequency while the natural frequency (and its subharmonic) are suppressed. The presence of serrations in the trailing edge creates a spanwise pressure gradient, which is responsible for the development of a secondary flow pattern in the spanwise direction. This pattern affects the mean flow in the near wake. It can explain an unexpected observation, namely that the velocity deficit downstream of a trough is smaller than the deficit after a protrusion. Furthermore, the insertion of serrations attenuates the energy of vortex shedding by de-correlating the spanwise coherence of the vortices. This results in weaker forcing of the separating shear layer, and both the subharmonic of the natural frequency as well as the shedding frequency appear in the spectra.

[a)]Email address for correspondence: nikitas.thomareis12@imperial.ac.uk

I. INTRODUCTION

Performance improvement of lifting devices has always been a challenge for the aerospace industry. Geometric modification of the wing section is one of the most common methods used to attain this goal. The absence of a complicated actuation mechanism has made passive control methods attractive, the most well known and widely used being the extendable flaps and slats employed since the first days of aviation. Since 1950s other methods have been studied, for example the truncation of the rear part of the wing to create a blunt trailing edge[1], leading to what is known as flatback profile. These early investigations showed the potential improvement of the maximum lift coefficient for the same flow conditions. More recent investigations have demonstrated additional benefits of the flatback airfoil, both experimentally and numerically[2–4], such as increased lift curve slope, optimized structural characteristics and decreased sensitivity to leading-edge transition. There benefits are important for low to medium Reynolds numbers applications, such as unmanned air vehicles or small wind turbines.

For small wind turbines in particular, blunt trailing edge airfoils offer significant advantages[2]. The cyclic gravitational and aerodynamic load results in large bending moments in the inboard region of the blades. This necessitates thick and structurally robust airfoil sections close to the hub, with thickeness to chord ratio larger than 25%. Thick airfoils with sharp trailing edges however have poor aerodynamic characteristics, while blunt trailing edges offer structural benefits without sacrificing the aerodynamic performance[2,5].

The exposed blunt part of the airfoil however leads to increased pressure drag due to shedding. For wind turbines, increased drag is not such an important issue for the inboard region of the blade[2]. Nevertheless, the benefits of blunt airfoils will increase if the penalty of increased drag can be mitigated. Biomimetics inspired several investigators to imitate the serrated geometries observed in animals such as whales or owls. Tanner et al.[6] used M-shaped serrations at the trailing edge of a blunt profile and found a decrease in the base pressure of up to 64% compared to the straight blunt trailing edge. Gai[7] found similar results with Tanner, and studied the effect of triangular serrations with angles of 60^o and 120^o, which were also shown to have positive effects. Rodriguez[8] investigated the effect of squared serrations on a 2D body and found a reduction of up to 40% of the total drag, with an additional study of the longitudinal vortices in the near-wake of the body and their effect

on the aerodynamics mechanisms. A more recent work by Krentel et al.[9] on a truncated NACA 0012 airfoil using various geometrical patterns, showed a decrease in the drag by 29% for a specific Reynolds number (44,000). The latest (experimental) study in this area by Nedić et al.[10], has shown that the effect of serrated trailing edges can be further improved by adding a self-similar repeating (i.e. fractal) pattern in smaller scales. It was shown that the single scale triangular serrations reduced vortex shedding and improved the lift-to-drag ratio for higher angles of attack, and that the addition of a fractal multiscale pattern reduced even more the shedding energy without affecting the improved aerodynamic characteristics.

A thorough study on the flow physics behind a bluff body with a sinusoidal trailing edge of constant thickness was made by Tompazis[11]. He found that the three-dimensionality effects in the wake can reduce the correlation length of the base pressure, causing a decrease in the pressure drag. Further investigation of the wake of bodies with spanwise undulation[12],[13] showed that the base pressure after the blunt trailing edge can be correlated to the frequencies of the vortex dislocations arising due to the spanwise inhomogeneity of the body. The aforementioned cases of bluff bodies with wavy trailing edges were also studied numerically with similar conclusions[14].

Most of the aforementioned investigations are experimental. As already mentioned, airfoils with modified trailing edges are suitable for low to medium Reynolds number applications, for which DNS is feasible. An important characteristic in the aerodynamic behavior of airfoils at moderate Reynolds numbers is the laminar separation, which occurs shortly after the leading edge of the airfoil, giving rise to a highly complex and dynamic field[15]. The behavior of the separated flow depends on the angle of attack, the Reynolds number and the type of the airfoil. Kotapati et al.[16] distinguish 3 different scenarios: attached flow at small angles of attack (case A), laminar separation, transition and reattachment (case B) and massively separated post-stall flow at high angles of attack (case C).

Most of the DNS studies of separating and transitional flows however have been performed on planar geometries[16–23]. The adverse pressure gradient required for the formation of a laminar separation bubble (encountered in real airfoils) is reproduced by a suitable boundary condition at the upper boundary of the computational domain. Several of these studies are concerned with the control of the laminar separation. There are only a few DNS studies on actual airfoils. The latter simulations are more challenging and require curvilinear (or unstructured grids), but are more realistic as the pressure gradient that results from the

interaction of the separation bubble with the potential flow around the airfoil and the Kutta condition is part of the solution and not imposed externally.

Shan et al.[24] performed DNS around a NACA 0012 at 4^o and Re based on the chord length equal to 10^5. The flow at these conditions corresponds to case B scenario. Indeed the authors captured the laminar separation, transition and reattachment of the shear layer. The shedding from the separated shear layer was attributed to the Kelvin-Helmholtz instability but no characteristic frequency was mentioned. Jones et al.[25] investigated the effect of forcing on the behaviour of a laminar separation bubble for a NACA 0012 at Re=50,000 and Mach 0.4. The forcing used in[25] was a single frequency volume forcing term applied in a predefined region, with an induced spanwise variation. They found that forcing improves the aerodynamic performance, requiring little energy input. A mechanism by which turbulence can sustain itself after the removal of forcing was proposed. Lehmkuhl et al.[26] investigated the capabilities of two sub-grid scale models suitable for unstructured grids for predicting the incompressible flow in transitional separating bubbles. A NACA 0012 airfoil with straight trailing edge was examined. DNS studies at $Re = 50,000$ were performed at two angles of attack, 5^o and 8^o, and used as reference to assess the performance of the sub-grid scale models. Recently DNS with Reynolds 400,000 were reported[27].

Simulations around airfoils with modified trailing edges are even more rare. Jones et al.[28] performed DNS simulations for a NACA 0012 with serrated trailing edge at the same Reynolds and Mach number as their previous investigation for a straight trailing edge[25]. A serrated plate with very small and uniform bluntness (equal to 1.2×10^{-3} times the airfoil chord) was appended to the straight trailing edge. Although the main focus of the paper was the study of the acoustic behavior of the airfoil, the analysis of the flow field close to the trailing edge revealed the breakup of large structures from the boundary layer as well as the creation of horseshoe vortices from the serrations. The same authors in another paper[29] found that the presence of serrations does not change the hydrodynamic field on the airfoil upstream of the serrations, including the behavior of the laminar separation bubble.

In the present paper, we investigate the effect of trailing edge modifications to the time average as well as the dynamic features of the flow. The central aim is to study the interaction of the separating shear layer with trailing edges of different shapes. We are interested only in the hydrodynamic effect of serrations and not their effect of the acoustic field. The modified trailing edges are obtained by removing material from the main body of

the airfoil, thereby exposing a finite bluntness, which is around 30 times larger compared to that of Jones et al.[28]. As will be seen later, this difference affects significantly the dynamics of the separating shear layer. We use the Dynamic Mode Decomposition (DMD) to identify the structures generated by the shear layer and the exposed bluntness.

The paper is organized as follows: the next section (II) provides details on the airfoils examined and computational method used, section (III) briefly describes the DMD method, section (IV) presents the resuls for the 3 airfoils examined and the last section (V) summarises the main findings of this work.

II. COMPUTATIONAL SET UP AND VALIDATION

The flow around three airfoils, all based on NACA 0012, was investigated with DNS. The airfoils had different trailing edge shapes: straight, truncated (blunt), and serrated. The airfoil with the straight trailing edge had a standard NACA 0012 cross section. The blunt trailing edge airfoil (also referred to as flatback airfoil below) was formed by truncating the NACA 0012 section at a distance $h = 0.133C$ from the trailing edge of the unmodified airfoil, thus exposing a uniform bluntness of thickness $\epsilon = 0.037C$. The airfoil with the serrated trailing edge is shown in Figure 1a. The serrations had triangular shape, exposing a bluntness that tapered linearly in the spanwise direction; it was maximum at the trough and zero at the peak. The maximum bluntness was equal to that of the flatback airfoil. A planar view of the trailing edge is shown in Figure 1b. Three geometric variables define the shape of the serrations: the height (h), the period (L) and the half-angle (ϕ), with values $h = 0.133C,\ L = 0.266C$ and $\phi = 45^o$.

For the discretization of the computational domain a C-grid topology was employed. The X, Y and Z coordinates are defined as follows: X is the free stream direction, Y is the cross-stream and Z is the direction along the span of the domain. The origin of the coordinate system is the leading edge of the airfoil.

The chord Reynolds number was $Re_C = 50,000$ and the angle of attack $\alpha = 5^o$. This combination results in laminar separation and turbulent reattachment and enables the study of the effect of the modified trailing edge on the separated flow features and the wake. Unless otherwise stated, frequencies are non-dimensionalised using free stream velocity U_∞ and the chord length C. For the airfoils with the modified trailing edges, the nominal chord length

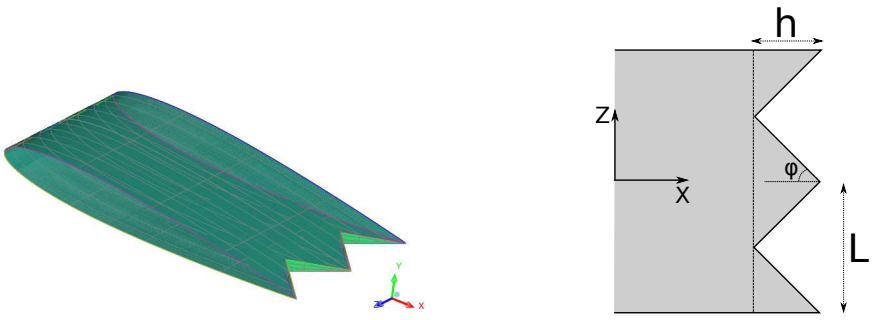

(a) Geometry of the airfoil with triangular serrations.

(b) Planar view of the trailing edge.

FIG. 1: Serrated trailing edge geometry and characteristic dimensions.

of the standard NACA 0012 profile from which they originate was used as a reference length.

An in-house code, called PantaRhei, was employed for the numerical simulations. The incompressible Navier-Stokes equations

$$\frac{\partial u_i}{\partial t} + \frac{\partial u_j u_i}{\partial x_j} = -\frac{\partial p}{\partial x_i} + \frac{1}{Re_C}\frac{\partial^2 u_i}{\partial x_j^2} \tag{1}$$

$$\frac{\partial u_i}{\partial x_i} = 0 \tag{2}$$

are solved using the Finite Volume Method (FVM) on a collocated, unstructured, grid. The convective terms are approximated with a 2^{nd} order central scheme. For time advancement, the second order backward differencing scheme is used. Viscous terms are treated fully implicitly. The convective terms are linearized by extrapolating u_j from the two previous time steps and treating u_i implicitly. Continuity is enforced via the Pressure Implicit with Splitting Operator (or PISO) algorithm[30]. The code is parallelised using the PETSc[31] library. For the solution of the pressure equation the GMRES method is employed together with the BoomerAMG algebraic multigrid preconditoner of the Hypre package[32].

The size of the computational domain in 3D must be large enough to capture the potential flow as accurately as possible, while at the same time minimising the computational expense. The domain of Jones et al[25] extends a radius $5.3C$ away from the airfoil and computations in a larger domain with radius $7.3C$ showed small variation in the pressure distribution. This modest domain size was found to be sufficient to capture the potential flow and this was attributed to the characteristics-based boundary conditions employed. The domain of Shan et al[24] extended $3C$ in the upstream and downstream directions and $4C$ in the cross-

stream direction; again a compressible flow solver was used with non-reflective boundary conditions in all boundaries. Zhang and Samtaney[33] and Lehmkuhl et al[26] employed larger domains, with radius of $10C$ and $20C$ respectively. In the present work, for the straight trailing edge airfoil, 3D simulations in two domains were performed. In the small domain, the inlet boundary is located $6.0C$ upstream of the leading edge, the outlet boundary $4.0C$ downstream of the trailing edge and the spanwise extent was $L_z = 0.1C$. In the larger domain, the inlet, top and bottom boundaries are located $18C$ away from the airfoil, the outlet boundary $20C$ downstream of the trailing edge, and the spanwise length is $0.2C$. Comparison between the results obtained from the two domains will be presented later.

For the blunt trailing edge simulations the spanwise extent was kept at $L_z = 0.2C$ in order to capture the 3D instabilities of the vortices emanating from the sharp trailing edge. These vortices scale with the edge thickness, ϵ, and are expected to develop 3D instabilities at the Re examined. Note that the Re based on ϵ is 1850, and 3D instabilities develop (at least for the flow around a cylinder) when Re is larger than about 190[34]. There are two types of instabilities (termed modes A and B) that have different spanwise length scales (4ϵ and ϵ respectively)[34]. The spanwise extent of $L_z = 0.2C$ is therefore wide enough to accommodate both instabilities. For the serrated trailing edge airfoil, the spanwise distance was two serration periods i.e. $L_z = 0.532C$.

The top and bottom surfaces were assigned free-slip conditions, while the side boundaries were periodic. The flow velocity was prescribed at the inlet, while at the outlet a one-dimensional convective boundary condition that employs the local cell velocity was used. This boundary condition allows the vortices to exit smoothly the computational domain with minimum reflection.

Grid resolution was very fine close to the airfoil, with 740 nodes around the surface (with appropriate clustering at the suction side to adequately resolve separation, transition and reattachment), 220 nodes at the wall-normal distance up to $0.15C$ and 500 nodes at the wake up to $2C$ downstream of the trailing edge. The number of layers along the span varied from 100 (for the straight trailing edge) to 140 (for the serrated trailing edge), leading to a total grid size between 50 and 70 million cells. The resolution in the wall-normal direction is at worse $\Delta y^+ < 1$ while for the streamwise and spanwise directions is $\Delta x^+ < 10$, $\Delta z^+ < 10$ respectively. After statistically steady behavior is reached, data are collected for a period of up to 40 time units (a time unit is defined as $tu = tU_\infty/C$).

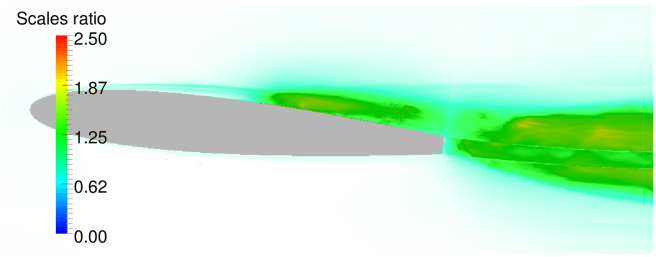

(a) Blunt trailing edge airfoil.

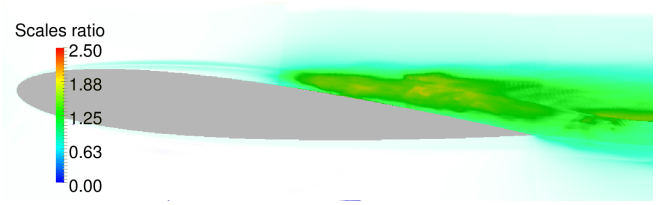

(b) Serrated trailing edge airfoil (plane through the peak).

FIG. 2: Contour plots of the the ratio of the characteristic grid size to the local Kolmogorov scale.

In order to assess the suitability of grid resolution for DNS studies, we computed the ratio of the characteristic cell size (defined as the cubic root of the cell volume) to the local Kolmogorov length scale i.e. $\frac{\sqrt[3]{V}}{\eta}$. Contour plots for this ratio for the blunt trailing edge and the serrated trailing edge airfoil (in a plane through the peak) are shown in Figure 2. It must be mentioned that the cell sizes in the XZ plane are the same for all 3 configurations (there are only minor differences to account for the different trailing edge geometry). As it can be seen, the ratio varies significantly and is maximal in the region of turbulent reattachment and the wake. In the largest part of the domain, the ratio is around 1 (or smaller) and there are very small regions for which the ratio is around 2 or slightly larger (the max value is 2.5). Resolution requirements for a proper DNS have been reported in Moin and Mahesh[35], Donzis et al.[36]. The latter authors mention that a standard resolution for 2^{nd} order quantities (such as rms velocities or the energy spectrum which takes very small values and falls off rapidly at wavenumbers $k > 1/\eta$) is $\Delta x/\eta \approx 2$. It is expected therefore that the present mesh is sufficiently fine for the results to be true DNS.

In Figure 3, the spanwise autocorrelations of the streamwise velocity, R_{uu}, are shown for the straight (small domain) and the blunt trailing edge airfoil at 4 points (3 inside the

boundary layer and 1 in the near wake). The correlation curves depend on the selected point. The best decorrelation for both airfoils is obtained for the most upstream point, which is located before transition. For the other points the values reduce to small values at the middle of the domain. Zhang and Samtaney[37] computed the spanwise correlations for spanwise domain sizes that range from $0.1C - 0.8C$ and found that the results depend not only on the location selected, but also on the velocity component examined. In Figure 4 we compare the computed statistics with available results in the literature for the small and large domain for the straight trailing edge airfoil.

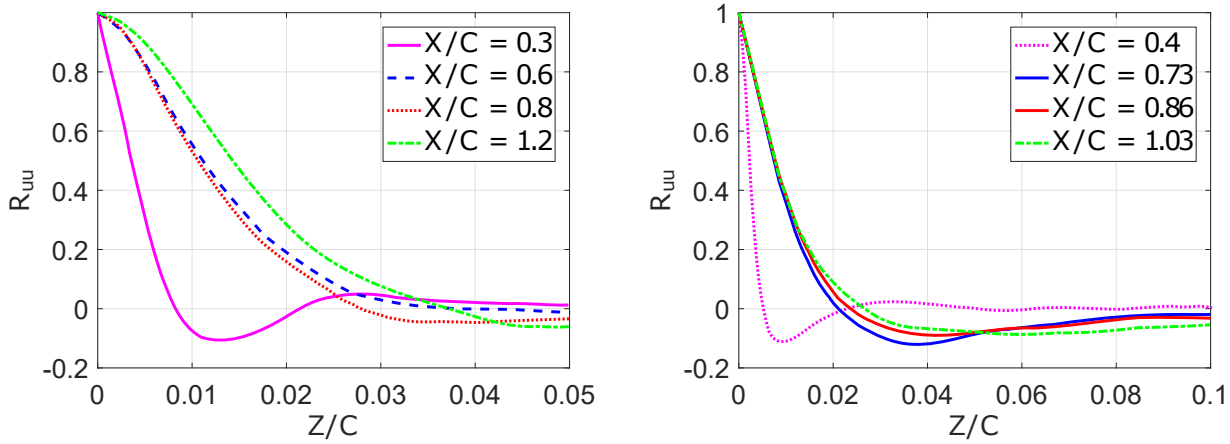

(a) Straight trailing edge ($L_z = 0.1C$). (b) Blunt trailing edge ($L_z = 0.2C$)

FIG. 3: Spanwise autocorrelation functions for the straight and blunt trailing edge airfoils. The first point is in the separation bubble, the 2^{nd} and 3^{rd} points are in the reattached turbulent boundary layer and the last points is in the very near wake. The cross stream coordinates of the points are for clarity mentioned here: for Figure 3a $Y/C = 0.038, 0.00037, -0.031, -0.075$ and for Figure 3b $Y/C = 0.025, -0.019, -0.041, -0.062$ going from the first to last point.

The DNS results of Lehmkuhl et al.[26] are ideal for such comparison. Figures 4a and 4b show the distribution of the pressure C_p and skin-friction C_f coefficients along the airfoil surface for the small and large domains. It can be seen that the effect of the domain size (between the two domains tested) is indeed negligible.

As far the comparison between the present results and those of Lehmkuhl et al.[26] is concerned, there are some small discrepancies, especially in the C_f coefficient, but overall

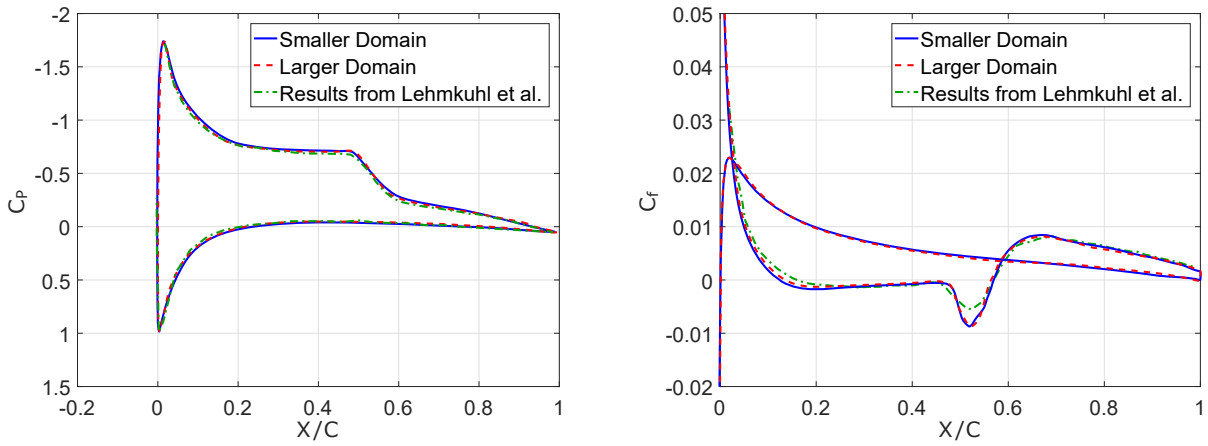

(a) Pressure coefficient C_p.

(b) Skin friction coefficient C_f.

FIG. 4: Comparison between the current results for C_p and C_f coefficients and the DNS results from Lehmkuhl et al.[26] .

the matching is reasonably good. The shape of the C_p profiles is very similar to that measured experimentally for laminar separation bubbles with transition followed by reattachment[38–40]. O'Meara and Mueller[38] identify the location of separation as the start of the constant-pressure region (also known as pressure 'plateau'), the free shear layer transition point as the end of the 'plateau', and the reattachment as the point at which pressure recovery exhibits a sharp decrease. These observations are broadly consistent with the C_p and C_f plots. The pressure 'plateau' appears to start a little downstream of the separation point, while the reattachement point matches with the position at which the rate of pressure recovery changes. Inspection of the Reynolds stress distributions (shown in the left column of figure 10) indicates that transiton starts at around $X/C = 0.45$, slightly upstream of the end of the pressure 'plateau'. The skin friction has very small values inside the recirculation region upstream of transition, which is consistent with the 'dead air region' of Horton[41]. Following transition, C_f reaches a minimum negative value, indicative of the 'reverse flow vortex'[41]. Increased momentum transfer due to turbulent mixing eventually eliminates the reverse flow and the flow reattaches at $X/C = 0.564$.

The separation and reattachment points as well as the force coefficients computed in the present work are compared with those from two other studies in Table I. There is good agreement with previously reported results. Small discrepancies do exist, but it must

	X_{sep}	X_{re}	C_L	C_D
Present	$0.145C$	$0.564C$	0.589	0.0271
Zhang and Samtaney[37]	$0.141C$	$0.58C$	0.562	0.0282
Lehmkuhl et al.[26]	$0.169C$	$0.566C$	0.569	0.0291

TABLE I: Comparison of time-averaged lift and drag coefficients C_L, C_D and separation and reattachment points X_{sep},X_{re}.

be borne in mind that the transition and reattachment locations are very sensitive to the numerical discretisation and mesh resolution. The lift and drag coefficients are also in reasonably good agreement with the results of Lehmkuhl et al.[26] and Zhang and Samtaney[37].

Figures 5a and 5b show the variation of streamwise velocity and turbulent kinetic energy across the boundary layer at three locations after reattachment (results obtained using the smaller domain). The profiles are compared with those of Lehmkuhl et al.[26] and again very good agreement is observed.

In Figure 6 instantaneous iso-surfaces of the Q criterion are shown for visualization of the flow separation and transition. The Q criterion was introduced by Jeong et al.[42] for visualisation of a vortex and it is defined as $Q = \frac{1}{2}(u_{i,i}^2 - u_{i,j}u_{j,i}) = \frac{1}{2}(||\mathbf{\Omega}||^2 - ||\mathbf{S}||^2)$, where $\mathbf{\Omega}$ and $\mathbf{S}$ are rotation and strain rate tensors respectively. When $Q > 0$ the rotation rate dominates the strain rate, and serves as a way to identify a vortex core. The periodic formation and break up of Kelvin-Helmholtz vortices is clearly seen in the figure. The break up, at this particular time instant, starts to appear clearly at around $x/C = 0.50$, at the end of the pressure 'plateau' and the start of the rapid pressure recovery.

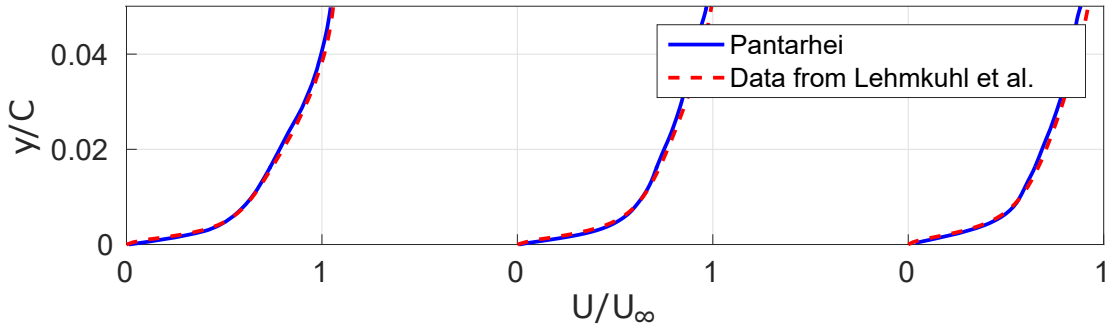

(a) Streamwise velocity profiles at 3 locations (from right to left $X/C = 0.7$, 0.8 and 0.9).

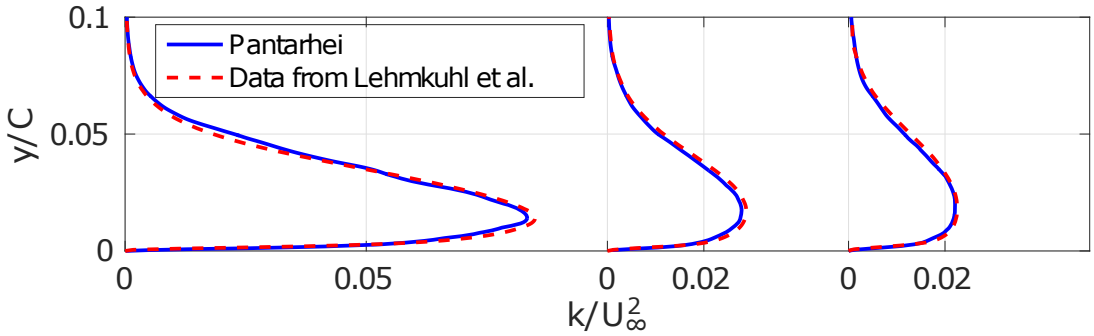

(b) Turbulent kinetic energy profiles at the same X/C locations.

FIG. 5: Comparison of profiles across the boundary layer.

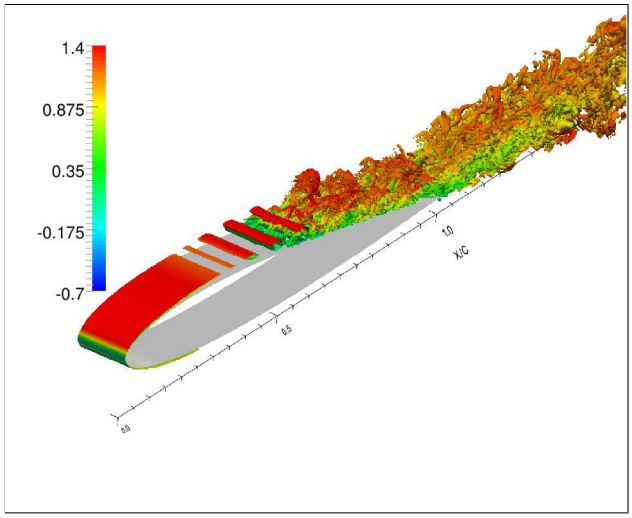

FIG. 6: Q contours in the range $[20, 100] \times (U_\infty/C)^2$ for the straight trailing edge case. The colorscale values are based on the streamwise velocity.

III. EXTRACTION OF DOMINANT MODES

Model reduction methods aim at reducing the complexity of flows by extracting and analyzing their most dominant modes (or structures). Proper Orthogonal Decomposition (POD) is the most widely used reduction method[43]. POD modes are mutually orthogonal and their amplitudes have multi-frequency content. This indicates that the spatial variation is decoupled from the temporal variation of the modes.

In the current work we use the Dynamic Mode Decomposition (DMD) method proposed by Schmid[44,45]. The method provides a set of non-orthogonal modes, each having a characteristic frequency. The temporal and spatial variations are therefore fully coupled. This method is more suitable than POD for the flow fields examined in the present paper, which are characterized by a set of few fundamental frequencies. It is therefore possible to extract directly the structures that oscillate at these frequencies. DMD has already been applied to different flows such as swirling jet[46] and flows around cylinders of different diameters[47] or around airfoils[48,49]. A brief description of the algorithm will be presented below, but for a more rigorous treatment we refer the reader to the original works of Schmid[44,45] and the analysis of Jovanović et al[50]. The review paper of Bagheri[51] provides a more general discussion on model reduction methods.

We assume a series of N time snapshots of the velocity field separated by Δt, $\mathbf{X}_1^N = \{\mathbf{v}_1, \mathbf{v}_2, ..., \mathbf{v}_N\}$. Each vector $\mathbf{v}_i$ is a column with the field data, for example the u and v velocity components in a 2D flow. We assume that each vector $\mathbf{v}_i$ has size M; usually $M \gg N$. The method assumes a linear dependence between consecutive snapshots of the form:

$$\mathbf{v}_{i+1} = \mathbf{A}\mathbf{v}_i \tag{3}$$

where $\mathbf{A}$ is the underlying (unknown) constant system matrix that describes the dynamic behavior of the system. If the differential evolution equation for variable $\mathbf{v}$ is $\frac{d\mathbf{v}}{dt} = \mathbf{B}\mathbf{v}$ then $\mathbf{A} = e^{\mathbf{B}\Delta t}$ and the aim of DMD is to extract the eigenvalues and eigenvectors of matrix $\mathbf{B}$ using the field snapshots. If we define matrix $\mathbf{X}_1^{N-1} = \{\mathbf{v}_1, \mathbf{v}_2, ..., \mathbf{v}_{N-1}\}$ then because of (3):

$$\mathbf{X}_1^{N-1} = \{\mathbf{v}_1, \mathbf{A}\mathbf{v}_1, \mathbf{A}^2\mathbf{v}_1, ..., \mathbf{A}^{N-2}\mathbf{v}_1\} \tag{4}$$

Combining (3) and (4) we get

$$\mathbf{X}_2^N = \mathbf{A}\mathbf{X}_1^{N-1} \tag{5}$$

where $\mathbf{X}_2^N = \{\mathbf{v}_2, \mathbf{v}_3, ..., \mathbf{v}_N\}$.

The economy-size SVD (singular value decomposition) of $\mathbf{X}_1^{N-1}$ is $\mathbf{X}_1^{N-1} = \mathbf{U}\mathbf{\Sigma}\mathbf{V}^*$ (* denotes the conjugate transpose of a matrix), where $\mathbf{\Sigma}$ is a diagonal $(r \times r)$ matrix that contains the r non-zero singular values (i.e. r is the rank of $\mathbf{X}_1^{N-1}$), $\mathbf{U}$ and $\mathbf{V}$ are matrices with ortho-normal columns ($\mathbf{U}^*\mathbf{U} = \mathbf{I}$ and $\mathbf{V}^*\mathbf{V} = \mathbf{I}$) and dimensions $(M \times r)$ and $(r \times N)$ respectively.

If $\mathbf{A}$ is expressed as $\mathbf{A} = \mathbf{U}\mathbf{F}\mathbf{U}^*$ then it can be shown[50] that matrix $\mathbf{F} = \mathbf{U}^*\mathbf{X}_2^N\mathbf{V}\mathbf{\Sigma}^{-1}$ minimises the Frobenious norm $\parallel \mathbf{X}_2^N - \mathbf{A}\mathbf{X}_1^{N-1} \parallel_F^2$. The eigenvector $\boldsymbol{\phi}_i$ of $\mathbf{F}$ is related to the eigenvector $\mathbf{y}_i$ of $\mathbf{A}$ by $\mathbf{y}_i = \mathbf{U}\boldsymbol{\phi}_i$. The reconstructed flow field $\tilde{\mathbf{v}}_j$ $(j = 1 \dots N-1)$ is given by

$$\tilde{\mathbf{v}}_j = \sum_{i=1}^{r} \mathbf{y}_i \ (\lambda_i)^j \ \alpha_i \tag{6}$$

where α_i is the amplitude of the i-th mode and λ_i the corresponding eigenvalue of $\mathbf{F}$. In order to compute the amplitudes a second optimization problem is solved[50].

When applied to a linear system, equation (3) is exact. In this case, the computed modes/eigenvalues represent the physically correct structures and their growth rates, frequencies. For non-linear systems, (3) represents a best linear map that links all snapshots. If the flow is characterized by periodically repeatable and persistent (i.e. neutrally stable) structures, the DMD method should be able to detect these and the associated frequencies. For these structures, the growth rate (i.e. the magnitude of λ) should be very close to 1, which indicates that they are neutral. A large value of the amplitude, α_i, is not a reliable indicator for the selection of such structures, as it may characterise a mode that will eventually decay. For this reason, the amplitudes α_i are multiplied by $(\lambda_i)^{N-1}$, so that modes with high α_i but $|\lambda_i| < 1$ (i.e. higher damping ratios) are not prominent.

IV. RESULTS AND DISCUSSION

In this section results are presented starting with the straight trailing edge, followed by the flatback and ending with the serrated edge. This order of exposition helps to understand better the process of interaction of the trailing edge with the separating shear layer.

A. Airfoil with straight trailing edge

The DMD method was applied on a Z plane at the mid span, in an $X-Y$ window with dimensions $[-0.2, 2] \times [-0.27, 018]\, C$. In total $N = 300$ time snapshots separated by $\Delta T = 0.01^{C}/_{U_\infty}$ were used, which corresponds to approximately 12 shedding cycles. A polar plot of the computed eigenvalues is shown in Figure 7a. The modes appear in complex conjugate pairs and the ones with the largest amplitude $\alpha_i \left(\lambda_i\right)^{N-1}$ are marked with yellow colour. Two dominant modes can be identified from the DMD spectrum shown in Figure 7b: a low frequency mode located at $f_1 = 3.8$ and a high frequency at $f_2 = 7.4$.

In order to verify that these frequencies are indeed present and they are dominant, velocity time-signals from two different locations at the mid span were analysed: one on the suction side of the airfoil at $X/C = 0.53, Y/C = 0.032$ (inside the transitioning shear layer but upstream of reattachment) and one in the wake at $X/C = 2.0, Y/C = -0.17$. In Figures 8a and 8b the power spectral density of the cross-stream velocity is plotted. The velocity signal at the first point (Fig. 8a) shows a peak at the high frequency f_2 observed in Figure 7b. Note that in figure 8a the horizontal axis is linear and re-plotting using logarithmic axis (figure not shown) reveals that the energy content of the signal is distributed among a range of frequencies, centered around a broad peak at frequency f_2. Such a broad peak has also been observed experimentally[39,52] and is due to the fact that the shear layer amplifies a broad range of frequencies[53]. Similarly, the velocity signal at $X/C = 2.0$ (Figure 8b), shows a dominant peak located at the lower frequency f_1; again this is a broad peak due to the fact that the point is immersed in a turbulent wake.

The spatial structure of the two most dominant modes as well as the time averaged streamwise velocity field are depicted in Figure 9. In the time averaged field, shown in figure 9a, a thin recirculation zone can be clearly seen on the suction side of the airfoil. The high frequency, $f_2 = 7.4$, is associated with the Kelvin-Helmholtz instability triggered by the inflectional velocity profile across the separating shear layer[54]. As Figure 9b shows, this mode is dominant in the separating shear layer, approximately between $X/C = 0.4 - 0.8$. In the region where it is most dominant, the shear layer rolls up and sheds vortices, as shown in Fig 6.

It is difficult to compare directly this frequency against results from the literature because the flow conditions are different. For example, Jones[55] performed one-dimensional spatial

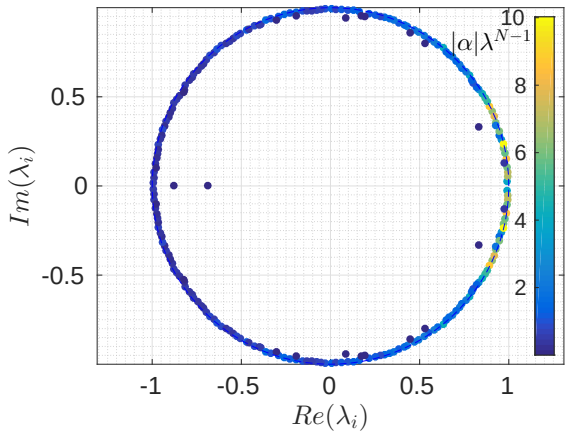

(a) Polar plot of the eigenvalues of each mode (color coded with the scaled amplitude).

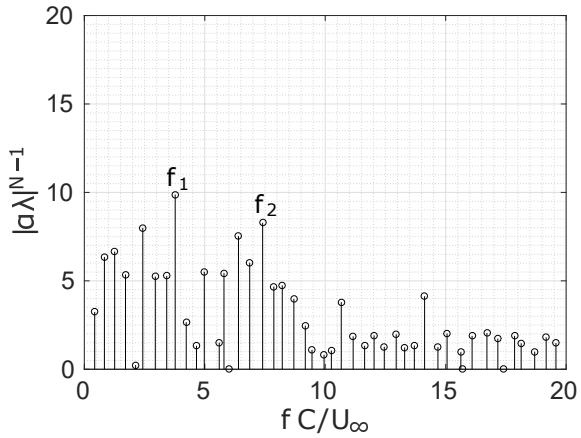

(b) Scaled amplitude distribution against frequency of the DMD modes.

FIG. 7: Amplitude distribution of the eigenvalues calculated from the DMD algorithm.

stability analysis on a number of time-averaged velocity profiles along the suction side for the same airfoil, angle of attack and Reynolds number, but with Mach number equal to 0.4, which makes compressibility effects non-negligible. The frequency with the strongest spatial growth slightly changes from one profile to the other, but overall the most amplified frequency in the shear layer was found to be $f = 8.49$, which is close to the present f_2. The difference can be attributed to two reasons: firstly, Jones's analysis is one-dimensional and is based on the Orr-Sommerfeld equation and, secondly, compressibility effects are expected to become more important in the area of high acceleration around the leading

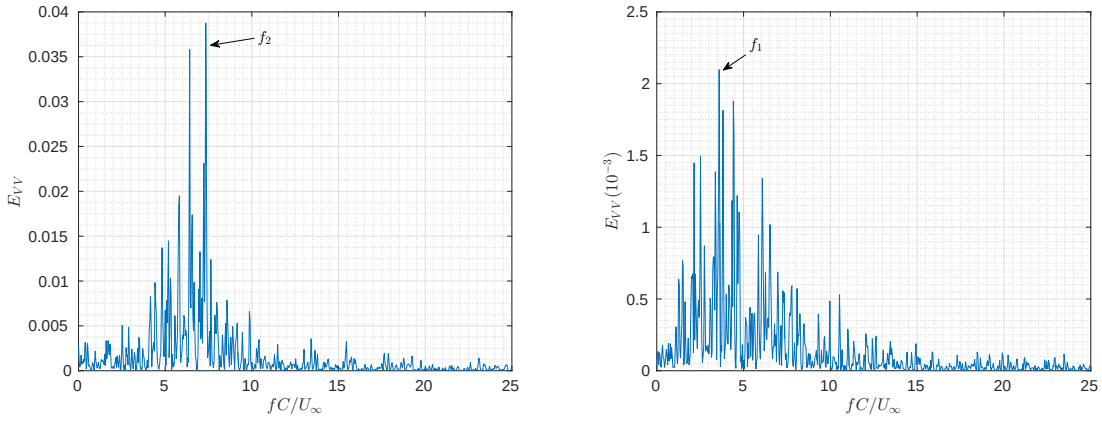

(a) (b)

FIG. 8: Power spectral density spectrum of the cross stream velocity component V at two different locations, $X/C = 0.53C, Y/C = 0.032$ (a) and $X/C = 2.0C, Y/C = -0.17$ (b).

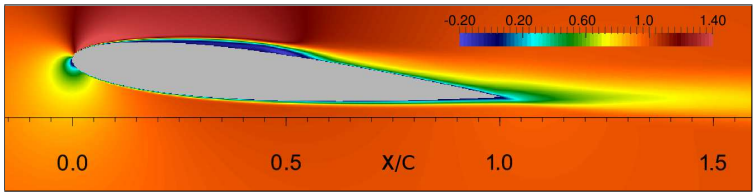

(a) Streamwise component of the mode corresponding to the mean flow.

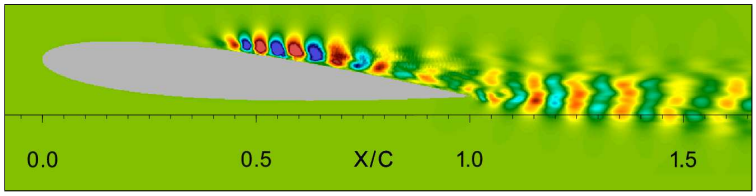

(b) Cross-stream component of the mode at f_2.

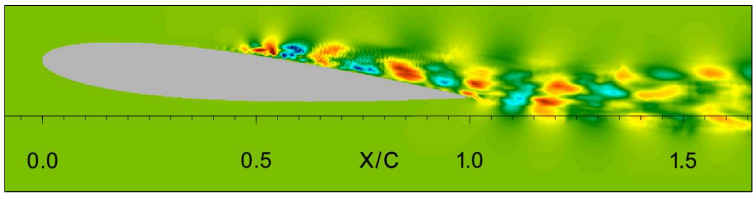

(c) Cross-stream component of the mode at f_1.

FIG. 9: Time-averaged streamwise velocity field (Figure 9a) and two most dominant DMD modes for a straight trailing edge (Figures 9b and 9c).

edge and therefore affect the velocity distribution of the separating shear layer and the most amplified frequencies. Boutilier and Yarusevych[39] examined the flow around a NACA 0018 at Re=100,000 and they also performed one-dimensional stability analysis using the measured time-averaged profiles. For the 5^o angle of attack, the dominant frequency was found to be 13.0 (table II in their paper). The difference with the present work can be attributed to the different Reynolds number (there is a power law dependency of the shear layer frequency and Reynolds number)[40] and the different thickness of the airfoil that affects the velocity distribution in the suction side.

The predicted frequency, f_2, however is in agreement with previous results when non-dimensionalized with the appropriate length and velocity scales. Huang and Ho[56] and Yarusevych et al.[52] have identified the streamwise distance of the shed vortices, ψ_0, and the velocity at the edge of the boundary layer at the point of separation, U_{es}, as the relevant length and velocity scales respectively. The distance ψ_0 can be directly estimated from the spatial structure of the DMD mode (Figure 9b) and it is found to be $\psi_0 \approx 0.08C$, while $U_{es} = 1.4U_\infty$. The corresponding non-dimensional frequency is $f_2^* = f_2\psi_0/U_{es} \approx 0.44$, very close to the observed range of values $0.45 - 0.5$[52].

It is known that as the amplitude of the perturbation grows spatially, non-linear interactions result in a lower frequency, which is a subharmonic of the fundamental instability frequency (for the mechanism of the generation of the subharmonic refer to the review paper of Ho and Huerre[53] and references therein). The DMD method captures a low frequency at $f_1 = 3.8$. The footprint of this frequency is shown in figure 9c. The mode is activated at $x \approx 0.45C$ (slightly downstream compared with the high frequency mode) and is seen to be present in the reattaching shear layer and the near wake, before decaying slowly further downstream. This frequency is indeed very close to the subharmonic of the fundamental frequency $f_2/2 = 3.7$ (the difference is 2.7%).

In the left column of Figure 10 contour plots of the three normal components of the Reynolds stresses are shown. The same color scale is used to facilitate comparison of the plots. Rapid growth of fluctuations starts at about $X/C = 0.45$ indicating transition to turbulence, as already mentioned. Shortly afterwards is the location of the start of rapid pressure recovery shown in the C_p plot (Figure 4a) and the location of the minimum value of the skin friction (Figure 4b). Close to the reattachment point ($X/C = 0.56$) all three normal components attain very large values. After the peak, the Reynolds stresses decay

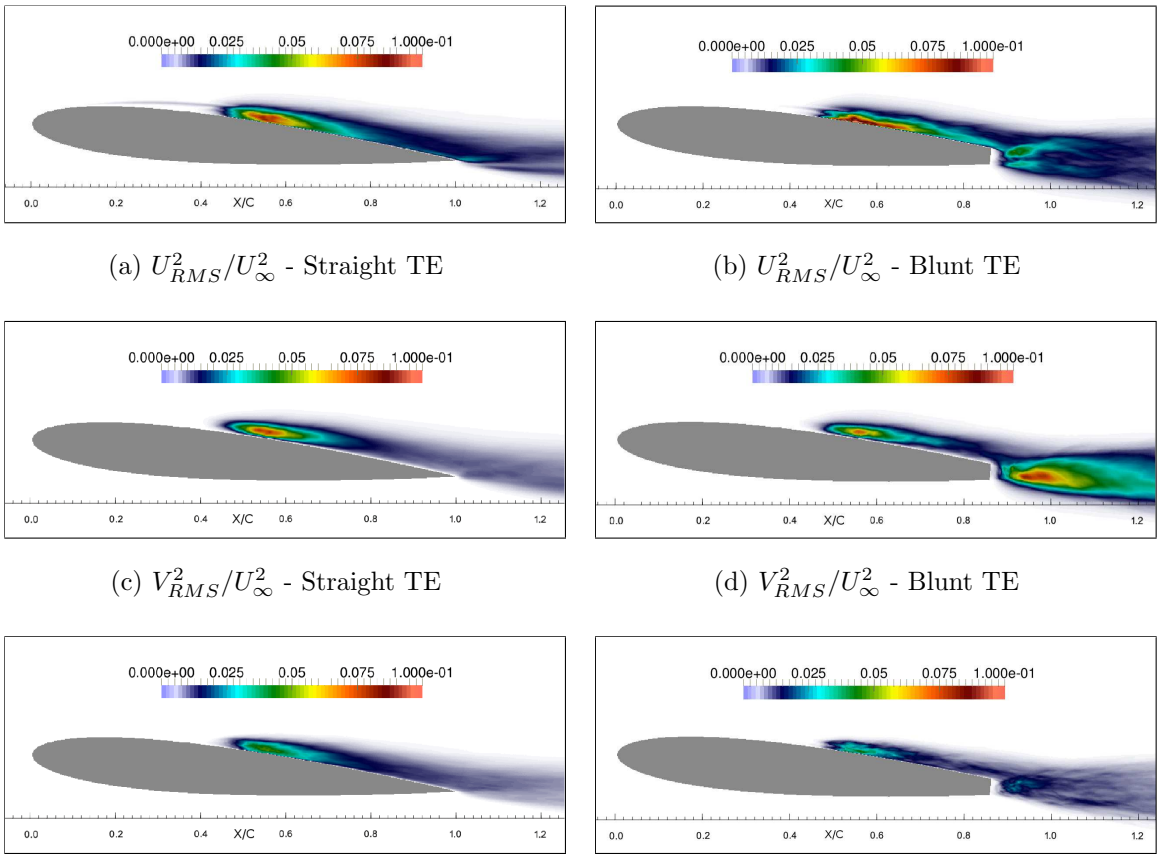

(a) U^2_{RMS}/U^2_∞ - Straight TE

(b) U^2_{RMS}/U^2_∞ - Blunt TE

(c) V^2_{RMS}/U^2_∞ - Straight TE

(d) V^2_{RMS}/U^2_∞ - Blunt TE

(e) W^2_{RMS}/U^2_∞ - Straight TE

(f) W^2_{RMS}/U^2_∞ - Blunt TE

FIG. 10: Streamwise, cross-stream and spanwise Reynolds stress distributions for the straight and blunt trailing edge airfoils.

downstream. Note also that strong spanwise velocity fluctuations appear denoting the rapid 3D breakdown of the vortices. Two dimensional simulations for this Reynolds number and angle of attack therefore do not describe accurately the flow.

B. Airfoil with blunt trailing edge

The DMD method was applied again on the mid-span plane in the same $X-Y$ window as in the straight trailing edge case i.e. $[-0.2, 2] \times [-0.27, 0.18]\, C$. In total 240 time snapshots, separated by $\Delta T = 0.01 {}^{C}/_{U_\infty}$, were used, which correspond to 11 shedding cycles. The DMD spectrum in this window is shown in Figure 11. One very dominant frequency appears at $f_{bl,1} = 4.5$. Its first harmonic at $f_{bl,3} = 2f_{bl,1}$ also appears. The shear layer natural frequency identified previously is still present at $f_{bl,2} = 7.5$, albeit highly attenuated. It is clear that

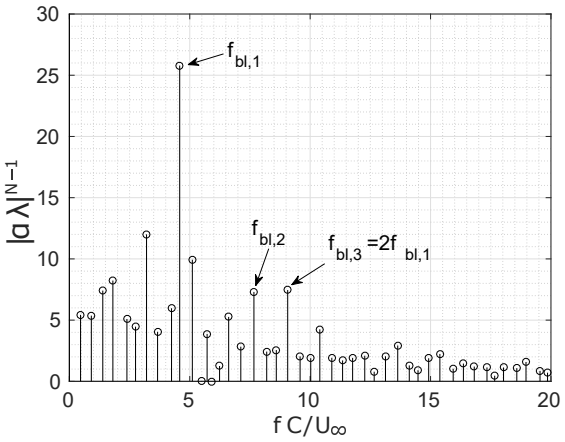

FIG. 11: DMD spectrum of the flow field around the blunt trailing edge airfoil.

the truncation of the trailing edge affects significantly the separating shear flow and its frequency content; this interaction will be examined in more detail below.

In Figure 12a contour plots of time-averaged streamwise velocity are shown. The flow in the suction side is qualitatively similar compared to the straight trailing edge airfoil: laminar separation, transition to turbulence, and reattachment. The locations of the separation and reattachment points are however different (at $0.23c$ and $0.58c$ respectively compared to $0.165c$ and $0.56c$ for the straight trailing edge) leading to a net reduction of the recirculation zone size. The most striking difference in the mean flows between the two airfoils is in the near wake: the presence of bluntness creates a small recirculation zone, which is absent in the straight airfoil case.

Inspection of Figure 13 demonstrates that the pressure distribution in the separating shear layer is also different. The minimum C_P is -1.72 for the straight trailing edge, and -1.59 for the blunt trailing edge. To identify the origin of this difference, potential flow simulations with Xfoil[57] were performed and exactly the same behavior was observed; the origin therefore is inviscid. This difference has been also observed in the past by Chen et al.[58] and it is a direct effect of the truncation of the trailing edge, which increases the radius of curvature of the leading edge in relation to the chord length.

Coherent structures originating from the truncated part of the airfoil are clearly illustrated in Figure 12b. This mode, corresponding to the frequency peak $f_{bl,1} = 4.5$, is characteristic of bluff body von Karman vortex shedding. Well-organized structures are shed from the truncated part of the airfoil and convect downstream without significant attenuation, at

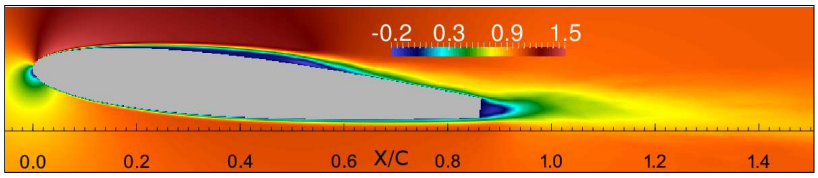

(a)

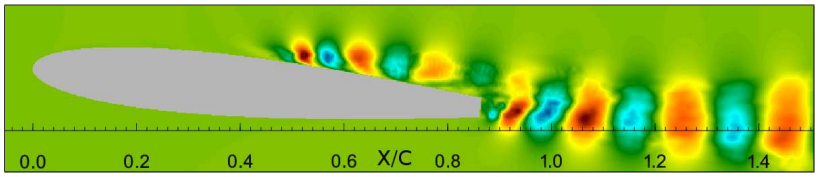

(b)

FIG. 12: Contour plots of the time-averaged velocity field U/U_∞ (12a) and the most dominant flow mode (12b) at $f_{bl,1}$.

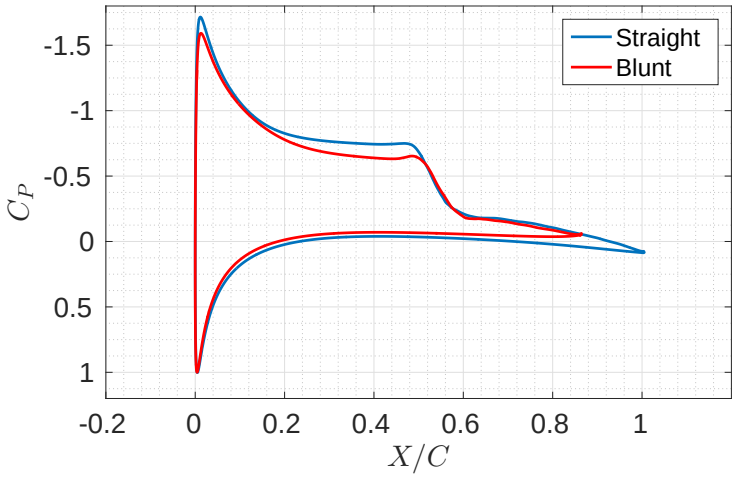

FIG. 13: Comparison of the pressure coefficients for the straight and blunt trailing edge cases.

least in the current field of view. The Strouhal number of this mode based on the trailing edge bluntness and the free stream velocity is $St_{bl,1} = 0.17$. The Strouhal number measured by Nédic et al.[10] was 0.189 for an identical geometry but with the chord based Reynolds number three times higher ($Re = 150,000$) and without laminar separation (both boundary layers were tripped). Krentel and Nitsche[9] found the shedding Strouhal number to be 0.2, but the Reynolds number based on the trailing edge thickness was 44,000, more than an order of magnitude higher compared to the one in the present paper (1,850). Although

this mode has the strongest presence in the wake, it's footprint extends far upstream in the suction side of the airfoil, as can be seen in figure 12b. This is not surprising. The wake shedding is the result of a global flow instability and therefore present in the whole flow field. This wake mode is therefore partially collocated with the separating shear layer and provides an excitation (forcing) to it. This has important implications as will be discussed below.

In order to confirm the dominance of the peaks identified in the DMD spectrum, Fourier analysis of the time signals from various probe points in the wake and the suction boundary layer was performed. In Figure 14, contour plots of the PSD of the cross-stream velocity spectra are plotted for three different streamwise locations. A strong peak can be identified at $f_{bl,1} = 4.5$, along with a weaker peak at the first harmonic $2f_{bl,1}$. These peaks are observed behind the trailing edge, they are elongated in the Y direction, are strongest close to the airfoil and attenuate downstream.

In Figure 15 the spectra at 6 points in the suction side boundary layer are plotted. A clear peak can be observed again at $f_{bl,1}$ at all locations. The maximum amplitude appears at Point B, inside the transitioning shear layer.

Both DMD and the spectra reveal a pronounced peak associated with the shedding frequency and it's harmonic. A third peak, with relatively reduced amplitude, can be observed in Figures 11 and 15 at frequency $f_{bl,2} = 7.5$. This peak is very close to the frequency $f_2 = 7.4$ of the straight trailing edge case and corresponds to the natural shear layer instability. Indeed, if the appropriate as before length and velocity scales are used, which for the blunt airfoil are $\psi_0 \approx 0.075C$ and $U_{es} = 1.34U_\infty$ respectively, the corresponding non-dimensional frequency $f^* = f_{bl,2}\psi_0/U_{es} \approx 0.42$, which is again close, albeit slightly below, the range of observed values[40]. Despite the presence of the natural instability, the shedding mode at $f_{bl,1} = 4.5$ is significantly more dominant, both in the DMD spectrum (Figure 11) and in the point spectra in the wake and suction side of the airfoil (Figures 14 and 15 respectively).

In order to investigate in more detail the behavior of the separating shear layer, the DMD method was applied on a smaller window on the suction side of the airfoil (see Figure 16b). The corresponding spectrum is shown in Figure 16a. Peaks at the same frequencies as in the spectrum of Figure 11 can be identified. The spatial structure of the mode corresponding to the peak at $f_{bl,1}$ is shown in Figure 16b. Distinct vortices originating from the separated shear layer can be identified. It appears that the trailing edge shedding affects the response

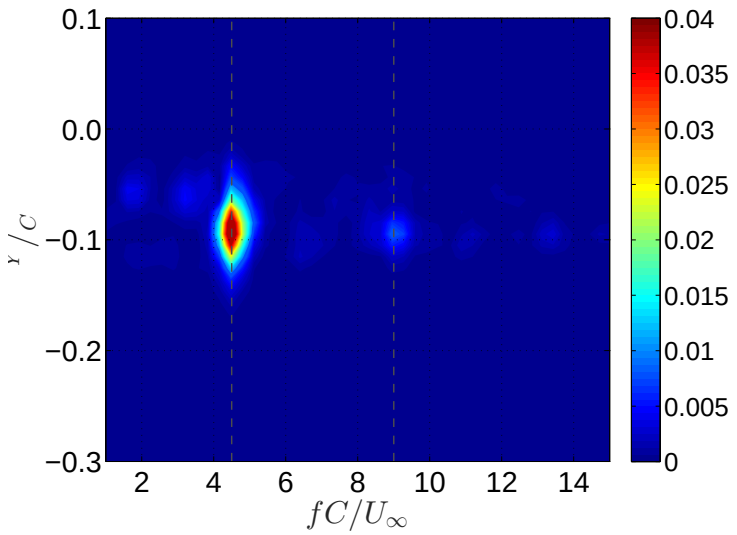

(a) Spectrum at $X/C = 1.05$.

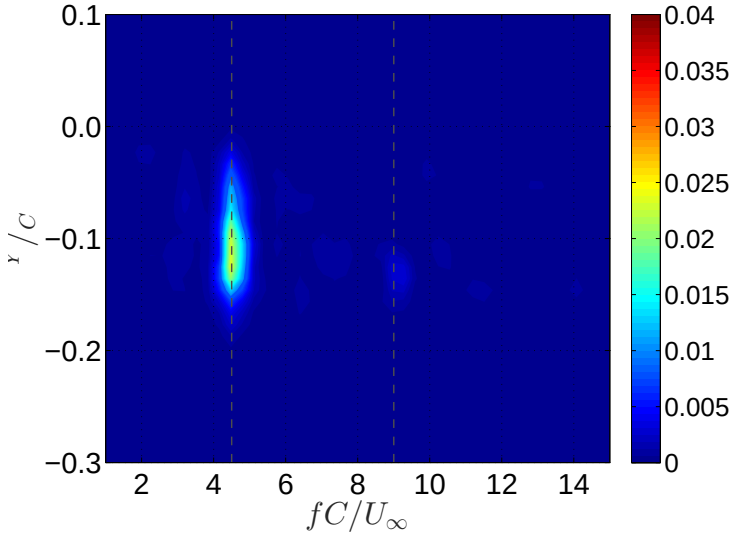

(b) Spectrum at $X/C = 1.4$.

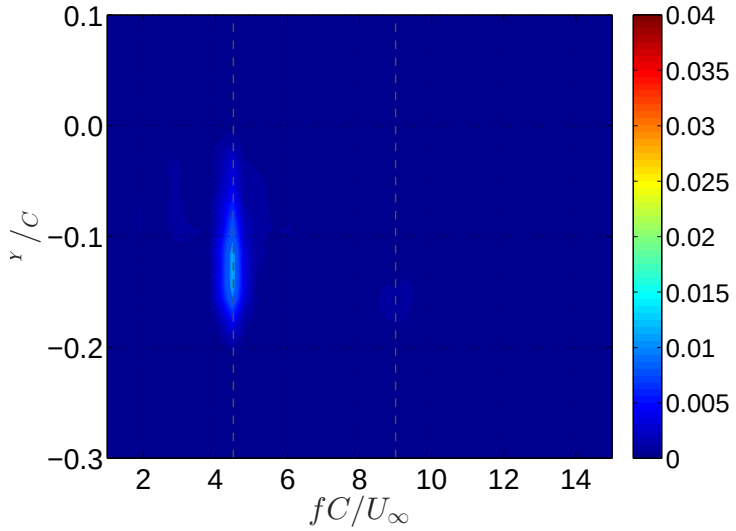

(c) Spectrum at $X/C = 2.0$.

FIG. 14: Spectra for the blunt trailing edge airfoil for different cross stream ($Y/C\big[-0.3, 0.1\big]$) and streamwise ($X/C = 1.05,\ 1.4,\ 2.0$) locations.

of the shear layer, by forcing it to oscillate and release vortical structures, at the same frequency. In other words, the shear layer is now locked to the shedding.

Previous works in the literature have examined the effect of forcing in the characteristics of separating shear layers but with an entirely different objective, namely that of control of separation. Marxen and Rist[18] looked at the mean flow deformation of a laminar separation

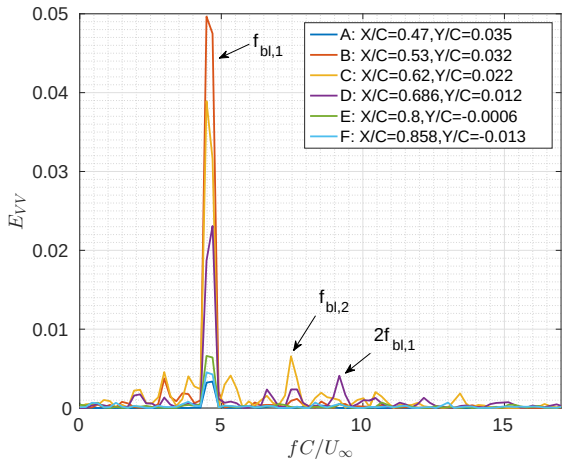

FIG. 15: Cross stream velocity spectra for 6 different locations at the suction side boundary layer, starting from $X/C = 0.47$ up to $X/C = 0.87$.

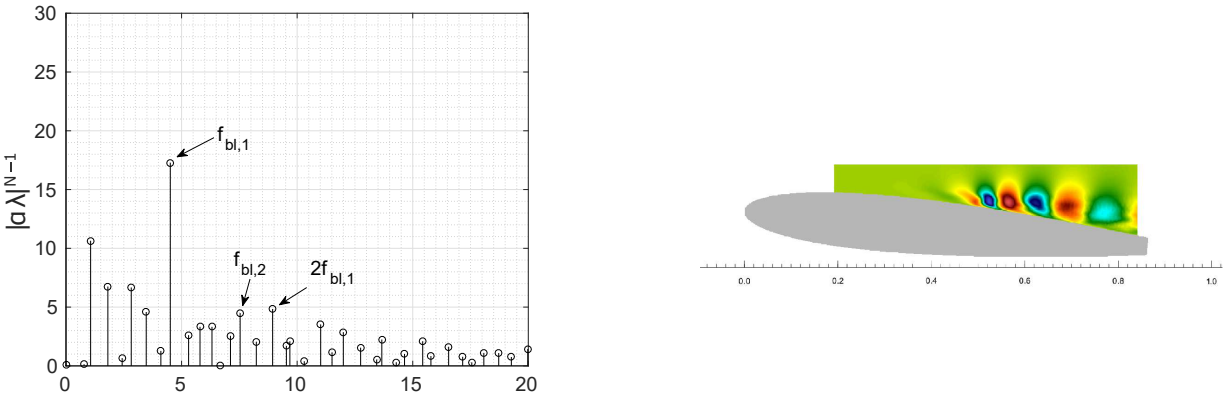

(a) (b)

FIG. 16: DMD spectrum (16a) and spatial structure of the mode at $f_{bl,1}$ (16b) at the plane capturing the shear layer transition and reattachment. The cross-stream component of the mode is plotted.

bubble that develops in a flat plate due to harmonic forcing upstream of the bubble. They noticed a reduction in the size of the bubble and a stabilisation of the flow with respect to small linear perturbations. Similar were the findings of Rist and Augustin[19]. Greenblatt and Wygnanski[59] have writtten an extensive review on the subject. The difference with the present work is that periodic perturbations aiming at separation control are imposed externally and upstream of the separation bubble. In our case however, they appear naturally due to the vortex shedding from the blunt trailing edge, they are strongest in the near wake,

but they have strong upstream influence.

The response of a free shear layer to external forcing has been studied by Ho and Huang[60], where it was found that the shear layer showed different states of lock-in depending on the ratio f_f/f_n, where f_f is the frequency of the external forcing and f_n the natural frequency of the shear layer. For our case, this ratio is $4.5/7.5 = 0.6$, i.e the forcing frequency is close to the subhamonic. Ho and Huang[60] have shown that this ratio is well within the region where the frequency response of the shear layer is expected to be the same as the forcing frequency. This is exactly what we find in our simulations.

Vortex shedding has also appeared in many experiments, however the ratio of the shear layer frequency to the vortex shedding frequency is quite large. For example in the experiments of Yarusevych et al[52], for the range of Reynolds numbers for which reattachment occured, this ratio was at least 7. There is one study in which these two frequencies are similar, that of Kotapati et al.[16]. The authors studied a flow configuration with laminar separation, reattachment and vortex shedding. There are however some important differences compared to our case: first, instead of an airfoil, they examined a flat plate with elliptic leading edge and a blunt trailing edge (with thickness 5% of the chord) at zero incidence, and secondly, they induced the laminar separation bubble close to the trailing edge, in the aft one-third of the flat plate. They report a shear layer instability frequency equal to 7.3 (surprisingly close to ours) and a vortex shedding frequency of 5.0 (obtained when there was no separation bubble, again not far from ours). Their 2D simulations showed that the shear frequency and the shedding locked to a single frequency of 2.9, while we find locking at a larger frequency (equal to 4.5). The explanation for this difference is the following: the authors induced the separation bubble close to the trailing edge (the reattachment point is located at $0.97C$), therefore the effective length scale for the vortex shedding (in essence, the effective thickness seen by the flow) is the sum of the plate thickness and the height of the separating bubble[16] (equal to $0.037C$ and located at around $0.88C$, as can be observed from their figure 5). In our case the separation bubble appears in the middle of the airfoil, the flow reattaches at $0.56C$, so the thickness of the bubble does not affect the effective length scale of shedding. In order to confirm that this is indeed the case, we performed an additional DNS simulation in which the boundary layer was tripped numerically at the region $X/C = 0.03 - 0.04$. The tripping resulted in a quick transition to an attached turbulent boundary layer on the suction side of the airfoil, and the shedding frequency was also 4.5.

This confirms that the presence of separation bubble does not affect the shedding frequency, and the latter is due only to the bluntness. The shear layer then locks to the externally imposed frequency and that frequency depends only on the thickness of the trailing edge.

There is one more aspect that needs clarification: Why the shear layer and shedding frequencies are similar, while in the other studies (excluding that of Kotapati et al.) the ratio is significantly higher, as already mentioned? The answer lies in the different length scales that generate the vortex shedding and in the particular value of the Reynolds number examined. More specifically, in the present case the characteristic length scale for the shedding is the trailing edge bluntness and not the thickness of body (as is, for example, in a thick NACA 0025 airfoil[52] or in a cylinder[34]); this has important implications for the shedding frequency. Reducing the characteristic length scale, increases the frequency (in order to keep the Strouhal number constant and relatively independent of the Reynolds number). In our case, the ratio of the trailing edge thickness to that of the airfoil is $\epsilon/t = 0.31$ resulting in a significant larger frequency, close to the subharmonic of the natural shear layer frequency. The latter has a power-law dependency on the Reynolds number[52] and, for the particular Re examined, it attains the value of 7.5, as aleady mentioned.

The Reynolds stress distributions are shown in the right column of Figure 10. The same scale is used for the straight and flatback airfoil. Significant differences are noticed, especially in the near wake. As expected for the flatback airfoil, the Reynolds stress distributions are similar to those created due to vortex shedding behind bluff-bodies. More specifically, the streamwise stress component, U^2_{RMS}, has two peaks close to the top and bottom edge of the blunt trailing edge (confirming that this is the correct length scale to use for the Strouhal number), while a single strong peak appears for the cross-stream component V_{RMS}. Both are results of the periodic formation and detachment of vortices from the top and bottom of surface of the exposed bluntness. A wider area of spanwise fluctuations, W^2_{RMS}, is also observed, which is a direct effect of the wider wake due to the Kármán shedding.

C. Airfoil with serrated trailing edge

The effect of adding the serrated trailing edge on the flow field will be examined in this section. As it will be shown, the flow field in this case is characterized by a three dimensional, secondary flow.

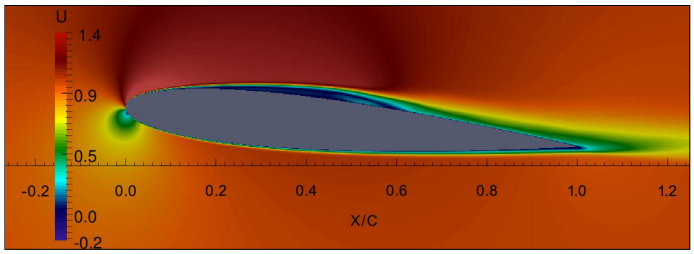

(a) Spanwise plane through the peak.

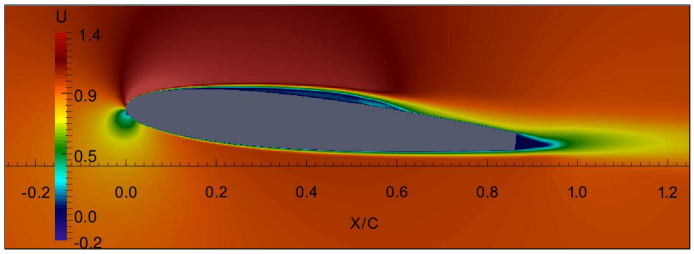

(b) Spanwise plane through the trough.

FIG. 17: Time-average streamwise flow fields through the peak and trough planes.

Attention is focused first on the characterisation of the spanwise inhomogeneity of the time-average flow. The streamwise flow fields at two planes (through the peak and the trough) are shown in Figure 17. The flow patterns in these two planes resemble the patterns around a straight and blunt trailing edge respectively.

Although not immediately evident from Figure 17 because of the color scale used, close examination of the velocity field in the near wake reveals an unexpected behaviour. Figure 18 shows profiles of velocity magnitude at 4 positions at the same streamwise distance ΔX from the trough and the peak locations. It can be clearly seen that the velocity deficits at the same distance from the airfoil surface are different. Most importantly, the wake deficit downstream of the peak is higher than the deficit downstream of a trough. At the location closest to the trailing edge, at $\Delta X = 0.1C$, the deficit after the peak is approximately 20% higher compared to the deficit after the trough. As ΔX increases, the relative difference diminishes and spanwise homogeneity is observed approximately one chord length downstream of the trailing edge. Due to the presence of bluntness at the trough base, one would expect a higher deficit downstream of the trough, and not the peak, at the same distance from the airfoil. This flow characteristic of the serrated trailing edge has also been observed experimentally by Prigent et al.[61].

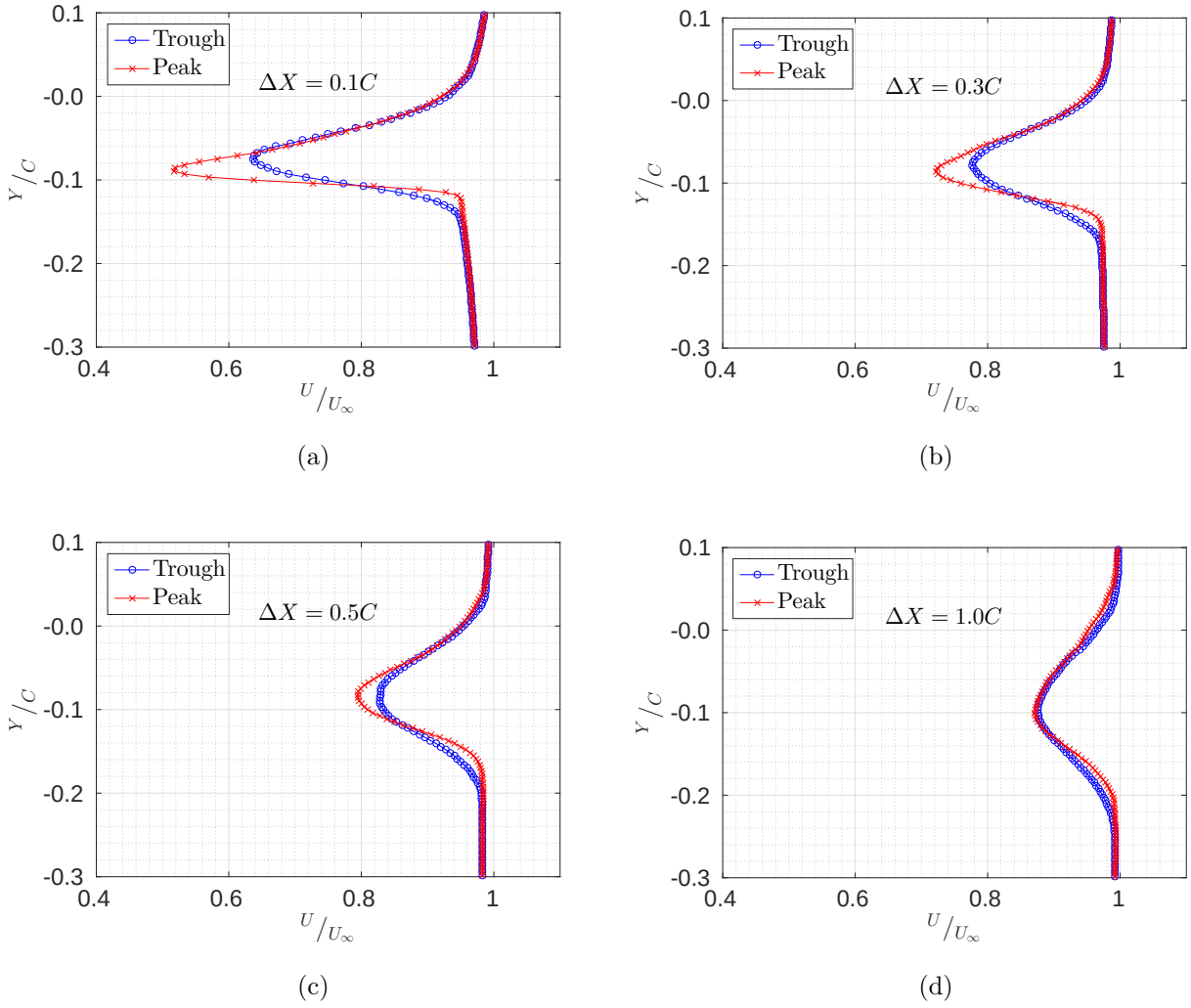

FIG. 18: Streamwise velocity profile at 4 different positions located at distance ΔX downstream of the trailing edge (ΔX is measured locally along the X direction from the trough and the peak spanwise locations).

In order to explain the flow acceleration behind the trough, we examine first the spanwise variation of the pressure distribution. Figure 19a depicts the surface pressure distribution trough the trough and the peak planes. It is clear that the pressure distribution is almost identical in the pressure and the suction side, with only small differences in the separating shear layer. The trailing edges however experience significant pressure difference. The static pressure at the peak is larger compared to the trough by about 10% of the dynamic pressure $\left(\frac{1}{2}\rho U_\infty^2\right)$. The reason for this pressure difference in the spanwise direction is not difficult to explain: after reattachment, the turbulent flow at the peak plane can recover pressure along

a larger distance, thereby reaching higher pressure at the trailing edge peak compared to the trough. Pressure varies also slightly inside the trough gaps (by less than 2% of dynamic pressure), as shown in figure 19b.

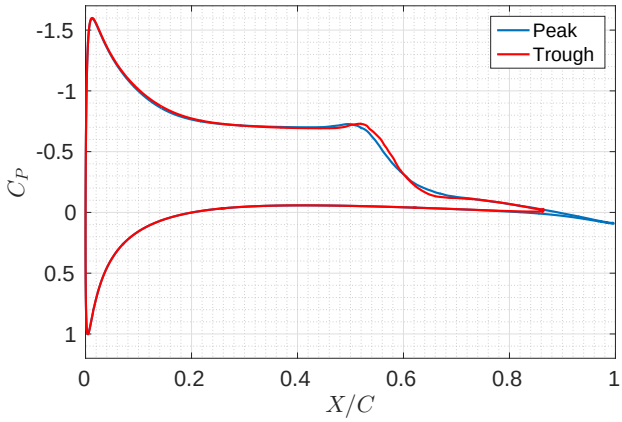

(a) Surface pressure distribution in the trough and peak planes.

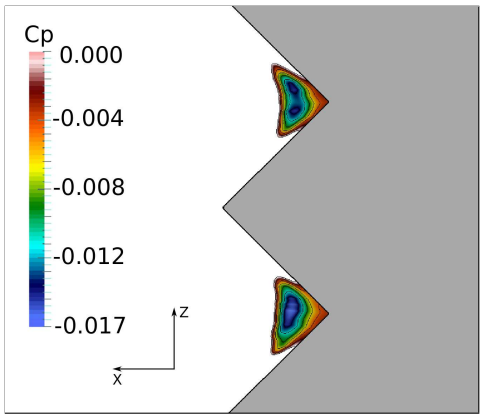

(b) Pressure inside the troughs.

FIG. 19: Pressure distributions on the airfoil surface and inside the troughs.

This spanwise pressure difference is responsible for the development of a secondary flow pattern. More specifically, the spanwise pressure gradient creates an undulating spanwise velocity component, W, as shown in Figure 20a. This velocity component is equal to 0 at the trough and peak locations (denoted by the dashed lines in figure 20a) and is maximized in the area in-between. It's value at the specific streamwise location shown is small, but close to the trailing edge increases, causing the time-averaged streamlines to bend towards the serration troughs, as illustrated in Figure 20b.

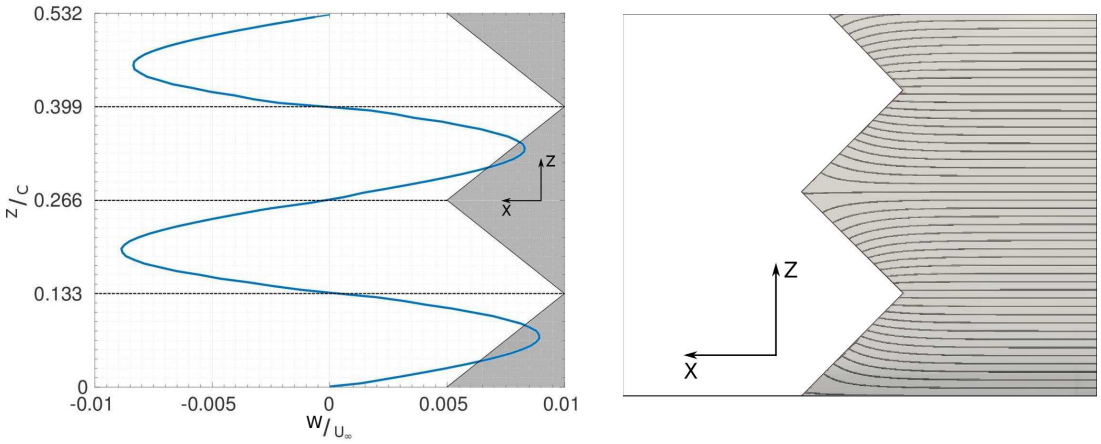

(a) (b)

FIG. 20: (a) Spanwise velocity component (W) along the span (pressure side of the airfoil, at distance $0.05C$ upstream of the trailing edge trough). The dashed lines indicate the positions where $W = 0$. (b) Time-averaged streamlines at the pressure side of the airfoil.

A three dimensional view of the time-averaged streamlines close to the trailing edge is shown in figure 21. The lines are color-coded with the streamwise velocity. The starting points for the generation of streamlines are placed at the pressure side of the airfoil. The streamlines are reminiscent of the flow generated from the wing tip vortices of a finite wing.

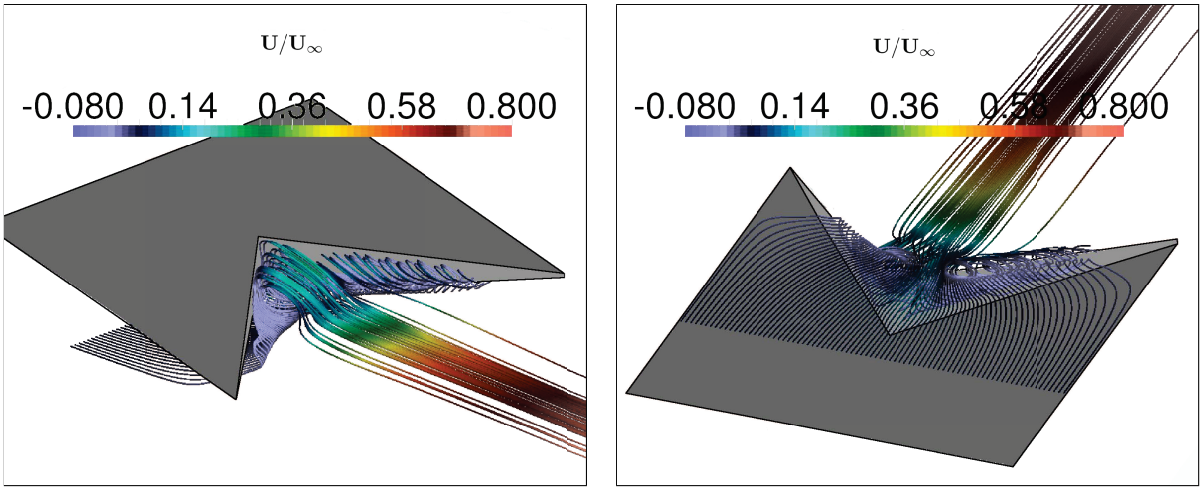

(a) Seed line placed at the pressure side of the airfoil (Top view)

(b) Seed line placed at the pressure side of the airfoil (Bottom view)

FIG. 21: Time averaged streamlines, color-coded with the streamwise velocity U/U_∞.

The low base pressure (due to the finite bluntness) creates a recirculating pattern along at the lip of the serration. The presence of the spanwise pressure variation and the W velocity component results in streamlines that spiral around the recirculation, transporting fluid from the peak to the trough. By virtue of the mass conservation, the flow in the trough is accelerated, thereby providing the mechanism that explains the aforementioned smaller velocity deficit oberved in the near wake.

Spectra are probed along the Y direction from $Y = -0.3C$ to $Y = 0.1C$ in $\Delta Y = 0.01C$ increments at three spanwise locations, directly after the trough, the mid-point and the peak (refer to Figure 22).

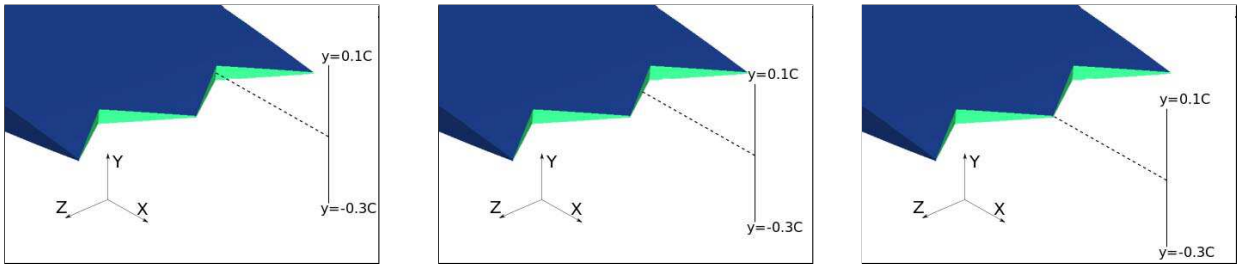

(a) (b) (c)

FIG. 22: Probing lines and their corresponding spanwise locations after the trough (a), the mid point (b) and the peak (c).

In Figure 23 spectra of the V velocity component (in the Y direction) are plotted. Each row corresponds to one spanwise location: directly after the trough, the mid-point and the peak (from top to bottom). Each column corresponds to one streamwise location: very close to the trailing edge at $X = 1.05C$ (left column) and at $X = 1.40C$ (right column). At the very-near wake ($X = 1.05C$) and directly after the trough two distinct peaks can be observed: one located at $f_{se,1} = 3.8$ and one located at $f_{se,2} = 4.4$. As we move towards the mid-point between the trough and the peak, the energy of both peaks reduces but they can still be identified. At the serration, the peaks still appear to exist, albeit significantly attenuated. The reduction in the peak energy as we move from the trough to the peak indicates a strong shedding inhomogeneity along the span of the airfoil.

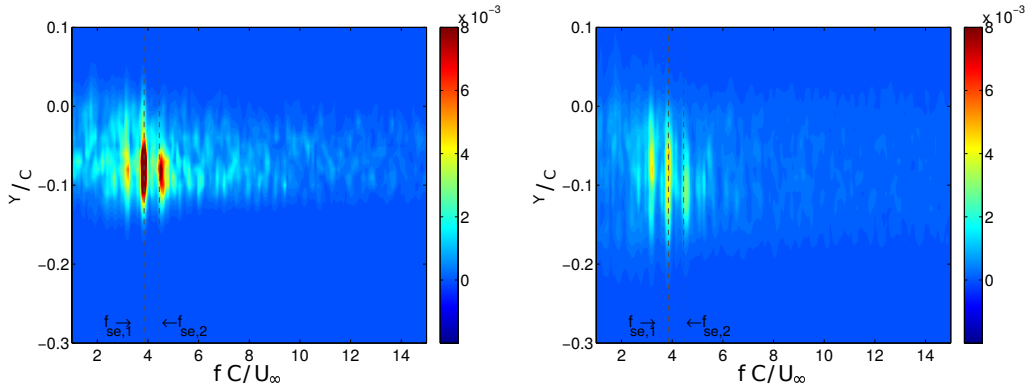

(a) Trough - $X = 1.05C$

(b) Trough - $X = 1.40C$

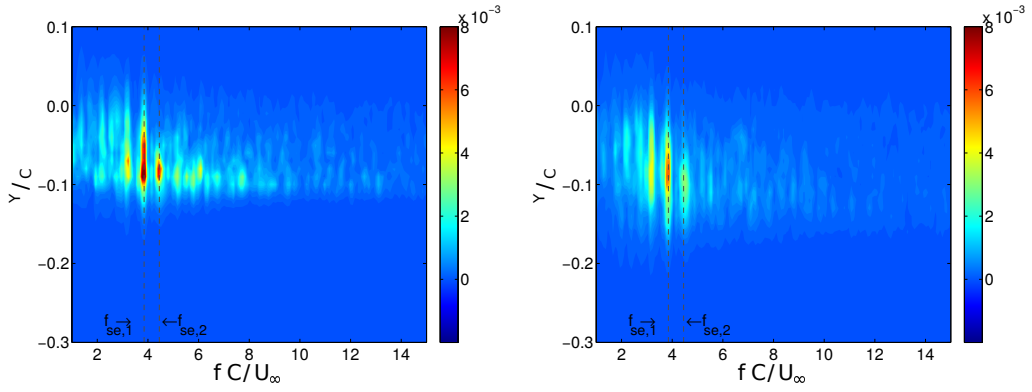

(c) Mid - $X = 1.05C$

(d) Mid - $X = 1.40C$

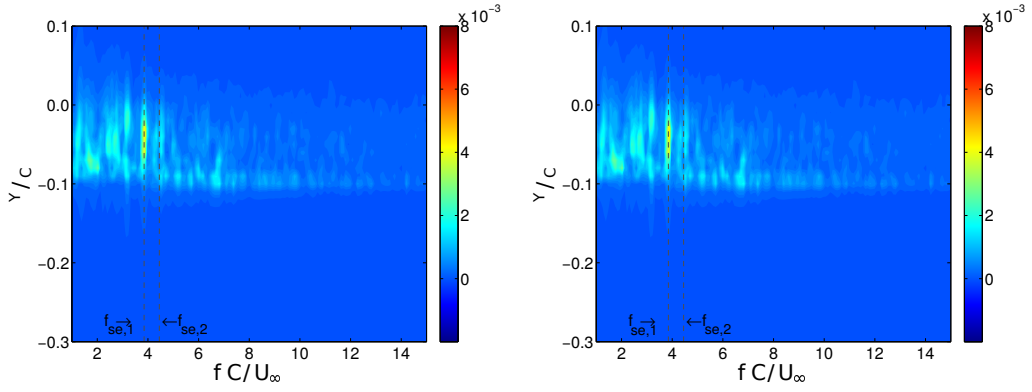

(e) Peak - $X = 1.05C$

(f) Peak - $X = 1.40C$

FIG. 23: Power spectra of V velocity component for different cross-stream locations, extending from $Y = -0.3C$ to $Y = 0.1C$. Left column data are probed very close to the trailing edge peak ($X = 1.05C$), while right column data are probed at $X = 1.40C$. From top to bottom, the probing lines are aligned with the trough, the mid-point and the peak of the serrations.

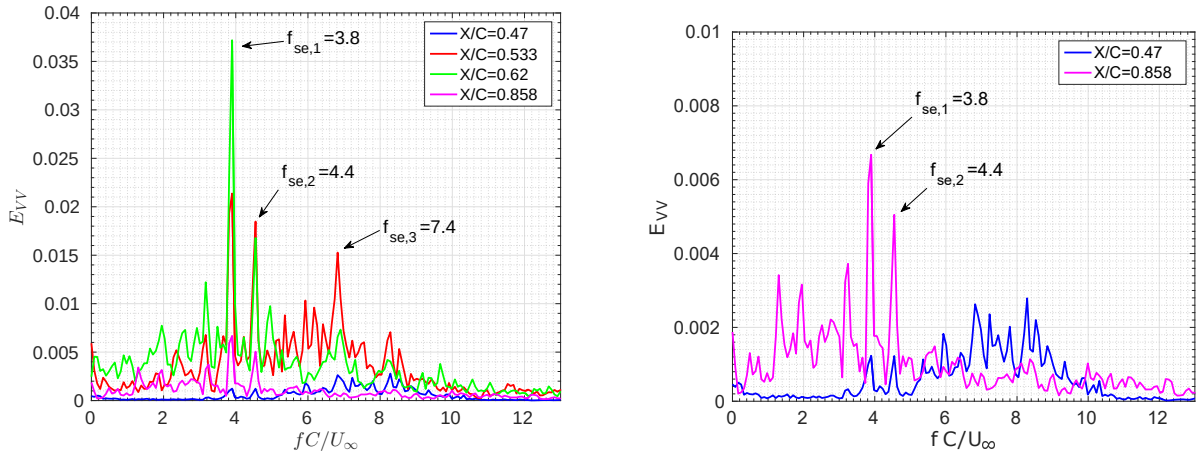

FIG. 24: PSD of the cross velocity component at four streamwise locations at the suction side of the airfoil at $Z/C = 0.266$ (plane through the peak). Figure 24b has zoomed in the region $E_{vv} \leq 0.01$ for better illustration of the signals at $X/C = 0.47$ and $X/C = 0.858$.

The two frequencies $f_{se,1}$ and $f_{se,2}$ are in almost perfect agreement with the dominant frequencies identified in the two previous airfoil cases. The dominant wake mode for the straight trailing edge was found to oscillate at $f_1 \approx f_{se,1}$, which was found to be the subharmonic of the natural frequency of the separating shear layer. The $f_{bl,1} \approx f_{se,2}$ frequency was found to be the shedding frequency of the flatback airfoil, which forced a lock-in between the shear layer and the wake shedding, as analysed in section (IV B). In the straight trailing edge airfoil only the subharmonic was present in the wake, while for the flatback only the shedding frequency was present. For the serrated case, both can be detected.

In Figure 24 the spectra for 4 different points in the suction side of the airfoil are plotted. All of the points are located at $Z/C = 0.266$, which corresponds to a plane through the peak. Figure 24b on the right has zoomed-in at the small values of E_{vv} for better visualisation of the spectra at two points. The first point at $X/C = 0.47$ shows a similar behavior to that in Figure 8a, namely a broad spectrum at relatively high frequencies. As the shear layer transitions, three peaks appear at the points located at $X/C = 0.533$ and $X/C = 0.62$. The peak at $f_{se,3} = 7.4$ is very close to the shear layer natural frequency observed at the straight trailing edge case, while the peaks at $f_{se,1}$ and $f_{se,2}$ are at the same frequencies already identified in Figure 23. At the fourth measurement point, at $X/C = 0.858$ i.e. directly

before the trailing edge, the peak at $f_{se,3}$ has completely attenuated and only $f_{se,1}$ and $f_{se,2}$ are still dominant, an observation in agreement with the wake spectra of Figure 23.

If the trough bluntness, ϵ, is used as a length scale, the Strouhal number corresponding to the frequency $f_{se,2}$ is $St = 0.1628$. Nédic et al.[10] studied a similar configuration and measured a Strouhal number equal to 0.203. However, the Reynolds number was three times larger and the boundary layers were tripped on both sides of the airfoil, as already mentioned. Due to tripping the boundary layers were attached, so Nédic et al.[10] detected only the trailing edge shedding frequency, $f_{se,2}$, and not $f_{se,1}$ which is due to the separating shear layer. This is fully consistent with the present findings.

Unlike the blunt trailing edge, where the shedding frequency was the only one present, in the serrated edge case we detect two distinct frequencies, the subharmonic of the natural frequency and the trailing edge shedding frequency. Why does the subharmonic frequency is observed for the serrated case and not for the blunt case? The reason is that the shedding for the serrated case is weaker due to the linear tapering of the thickness, from a maximum at the trough to almost zero at the peak. For the blunt trailing edge, the energy contained in the shedding frequency (figure 14) is 5 times larger than that for the serrated trailing edge (figure 23). This indicates that the forcing is much stronger for the blunt case, leading to a suppression of the subharmonic.

There are few other papers that have dealt with the flow around an airfoil with serrated trailing edges. Jones et el.[28] have studied similar flows, but there is an important difference, as already mentioned in the introduction: the serrations are attached to a straight trailing edge airfoil, and are not cut into the body of the airfoil. The thickness is therefore minimal and secondary patterns, as the one observed in this paper, were not reported.

In Figure 25 the normal Reynolds stresses are plotted for the serrated trailing edge airfoil. The left column shows the distributions at a spanwise plane through the serration peak, and the right column through the trough. The spanwise variation of the Reynolds stress distributions in the wake is clear. The wakes in the peak resemble those of the straight trailing edge airfoil shown in Figure 10 (left column), while in the trough plane the distributions are similar to those of the flatback airfoil (Figure 10, right column). There is however a significant difference in the V_{RMS} component in the wake. Comparison between Figures 10d and 25d reveals that the intense shedding from the blunt trailing edge, which gives rise to an elongated region of cross-stream fluctuations extending up to almost half

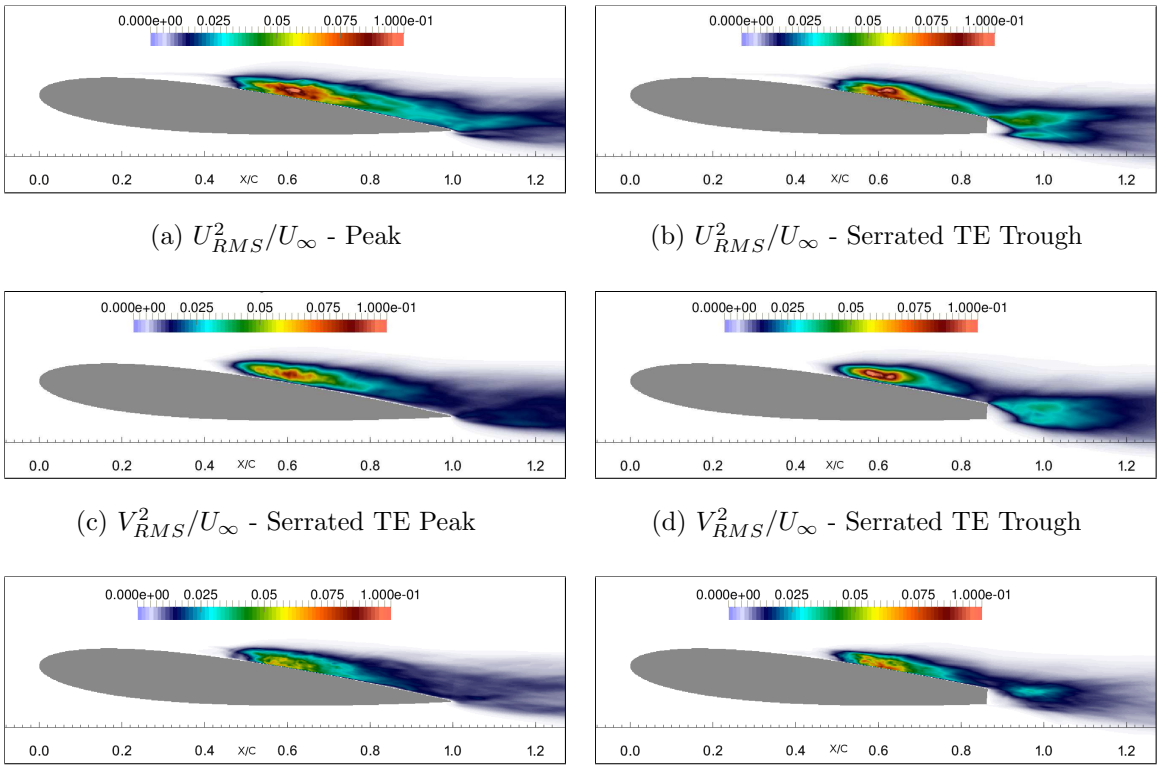

(a) U^2_{RMS}/U_∞ - Peak

(b) U^2_{RMS}/U_∞ - Serrated TE Trough

(c) V^2_{RMS}/U_∞ - Serrated TE Peak

(d) V^2_{RMS}/U_∞ - Serrated TE Trough

(e) W^2_{RMS}/U_∞ - Serrated TE Peak

(f) W^2_{RMS}/U_∞ - Serrated TE Trough

FIG. 25: Streamwise, cross-stream and spanwise Reynolds stress distributions for the serrated trailing edge airfoil at a spanwise plane through a peak (Figures 25a, 25c and 25e) and through a trough (Figures 25b, 25d and 25f).

a chord length downstream, is significantly attenuated in the serrated airfoil both in terms of magnitude as well as size. This indicates that the intensity of the wake shedding is reduced due to the presence of the serrations, and agrees with the previous discussion of the spectra. Experimental measurements[10] also confirm this behaviour. Another difference worth mentioning is the peak which appears in the spanwise velocity fluctuations W_{RMS} directly after the trailing edge trough (Figure 25f). This peak indicates a strong spanwise fluctuation of the flow field on this location, originating from the 3D secondary flow pattern discussed earlier in this section.

V. CONCLUSIONS

This paper considered the effect of trailing edge modifications on the time-average and dynamic characteristics of the separating shear layer and the near wake of a NACA 0012 airfoil. Two airfoils, one with blunt and the other with serrated trailing edge, were compared with a standard NACA 0012 airfoil with straight trailing edge. The DMD method was applied to extract the dominant modes in the wake and the corresponding frequencies. For the standard airfoil, two modes were detected: one with high frequency which corresponds to the Kelvin Helmholtz instability originating from the separating shear layer, and one with low frequency that emerges as a subharmonic, and is detectable in the suction side and the near wake.

In the blunt trailing edge airfoil, the two shear layer frequencies were strongly suppressed, and the frequency of the shear layer was locked to the shedding frequency due to the exposed bluntness. Examination of the spatial structure of the shedding mode revealed an upstream effect on the suction side of the airfoil. The shedding frequency was close to the subharmonic of the natural shear layer frequency and, under such conditions, lock-on is known to occur.

When the trailing edge consists of triangular serrations with tapering bluntness, the strength of the vortices shed from the exposed blunt part was strongly attenuated compared to the flatback airfoil. In this case, both the subharmonic and the shedding frequency were present in the velocity spectra, in the wake as well as in the suction side of the airfoil. In contrast with the flatback airfoil, in this case lock-in was not observed. This was attributed to the weaker forcing amplitude due to the decorrelation of the vortices shed along the span.

ACKNOWLEDGMENTS

This work was funded by the MULTISOLVE EU project (Grant Agreement Number 317269) under the ITN Marie Curie framework of the European Commission. The simulations were performed on Archer (to which access was provided through the UK Turbulence Consortium grant EP/L000261/1) and the CX2 facility of Imperial College. The authors would also like to thank Prof. C. Vassilicos for his useful comments on this work.

REFERENCES

[1]H. Smith and R. Schaefer, NACA Technical Note TN 2074, NACA (1950).

[2]K. Standish and C. Van Dam, Journal of Solar Energy Engineering **125**, 479 (2003).

[3]J. Baker, E. Mayda, and C. Van Dam, Journal of Solar Energy Engineering **128**, 422 (2006).

[4]H. Xu, W. Shen, W. Zhu, H. Yang, and C. Liu, in Journal of Physics: Conference Series (2014), vol. 524(1).

[5]R. Chow and C. van Dam, Wind Energy **16**, 445 (2013).

[6]M. Tanner, Tech. Rep., DTIC Document (1970).

[7]S. Gai and S. Sharma, Aeronautical Journal **85(844)**, 206 (1981).

[8]O. Rodriguez, Experiments in Fluids **11**, 218 (1991).

[9]D. Krentel and W. Nitsche, Experiments in fluids **54**, 1 (2013).

[10]J. Nedić and J. C. Vassilicos, AIAA Journal **53**, 3240 (2015).

[11]N. Tombazis, Ph.D. thesis, University of London Library (1993).

[12]P. W. Bearman and N. Tombazis, Journal of Wind Engineering and Industrial Aerodynamics **49**, 339 (1993).

[13]N. Tombazis and P. Bearman, Journal of Fluid Mechanics **330**, 85O112 (1997).

[14]J. Cai, T. L. Chng, and H. M. Tsai, Physics of Fluids (1994-present) **20**, 064102 (2008).

[15]P. Lissaman, Annual Review of Fluid Mechanics **15**, 223 (1983).

[16]R. Kotapati, R. Mittal, O. Marxen, F. Ham, D. You, and C. I. LN, Journal of Fluid Mechanics **654**, 65 (2010).

[17]M. Alam and N. D. Sandham, Journal of Fluid Mechanics **403**, 223 (2000).

[18]O. Marxen and U. Rist, Journal of Fluid Mechanics **660**, 37 (2010).

[19]U. Rist and K. Augustin, AIAA Journal **44**, 2217 (2006).

[20]O. Marxen, M. Lang, and U. Rist, Journal of Fluid Mechanics **728**, 58 (2013).

[21]O. Marxen and D. Henningson, Journal of Fluid Mechanics **671**, 1 (2011).

[22]D. Postl, W. Balzer, and H. Fasel, Journal of Fluid Mechanics **676**, 81 (2011).

[23]P. Spalart and K. Strelets, Journal of Fluid Mechanics **403**, 329 (2000).

[24]H. Shan, L. Jiang, and C. Liu, Computers & Fluids **34**, 1096 (2005).

[25]L. Jones, R. Sandberg, and N. Sandham, Journal of Fluid Mechanics **602**, 175 (2008).

[26]O. Lehmkuhl, I. Rodríguez, A. Baez, A. Oliva, and C. Pérez-Segarra, Computers & Fluids

84, 176 (2013).

[27]S. Hosseini, R. Vinuesa, P. Schlatter, A. Hanifi, and D. Henningson, in 15TH European Turbulence Conference (2015).

[28]L. Jones and R. Sandberg, Journal of Fluid Mechanics **706**, 295 (2012).

[29]R. Sandberg and L. Jones, Journal of Sound and Vibration **330**, 3818 (2011).

[30]R. I. Issa, Journal of computational physics **62**, 40 (1986).

[31]S. Balay, S. Abhyankar, M. Adams, J. Brown, P. Brune, K. Buschelman, V. Eijkhout, W. Gropp, D. Kaushik, M. Knepley, et al., Tech. Rep., Technical report, Argonne National Laboratory (ANL) (2014).

[32]R. D. Falgout, J. E. Jones, and U. M. Yang, in Numerical solution of partial differential equations on parallel computers (Springer, 2006), pp. 267–294.

[33]W. Zhang and R. Samtaney, Physics of Fluids (1994-present) **27**, 055101 (2015).

[34]C. Williamson, Annual review of fluid mechanics **28**, 477 (1996).

[35]P. Moin and K. Mahesh, Annu. Rev. Fluid Mech. **30**, 539 (1998).

[36]D. Donzis, P. Yeung, and K. Sreenivasan, Phys. Fluids **20**, 045108 (2008).

[37]W. Zhang and R. Samtaney, Computers & Fluids **124**, 39 (2016).

[38]M. O'Meara and T. Mueller, AIAA Journal **25**, 1033 (1987).

[39]M. Boutilier and S. Yarusevych, Physics of Fluids (1994-present) **24**, 084105 (2012).

[40]S. Yarusevych, P. Sullivan, and J. Kawall, Physics of Fluids (1994-present) **18**, 044101 (2006).

[41]H. Horton, Ph.D. thesis, Queen Mary, University of London (1968).

[42]J. Jeong and F. Hussain, Journal of Fluid Mechanics **285**, 69 (1995).

[43]G. Berkooz, P. Holmes, and J. L. Lumley, Annual review of fluid mechanics **25**, 539 (1993).

[44]P. J. Schmid, L. Li, M. Juniper, and O. Pust, Theoretical and Computational Fluid Dynamics **25**, 249 (2011).

[45]P. J. Schmid, Journal of Fluid Mechanics **656**, 5 (2010).

[46]Z.-H. Wan, L. Zhou, B.-F. Wang, and D.-J. Sun, European Journal of Mechanics-B/Fluids **51**, 16 (2015).

[47]P. Baj, P. J. Bruce, and O. R. Buxton, Physics of Fluids (1994-present) **27**, 075104 (2015).

[48]R. Dunne and B. J. McKeon, Experiments in Fluids **56**, 1 (2015).

[49]S. Mariappan, A. Gardner, K. Richter, and M. Raffel, AIAA journal **52**, 2427 (2014).

[50]M. R. Jovanović, P. J. Schmid, and J. W. Nichols, Physics of Fluids (1994-present) **26**, 024103 (2014).

[51]S. Bagheri, Archives of Computational Methods in Engineering **19**, 341 (2012).

[52]S. Yarusevych, P. E. Sullivan, and J. G. Kawall, Journal of Fluid Mechanics **632**, 245 (2009).

[53]C.-M. Ho and P. Huerre, Annual Review of Fluid Mechanics **16**, 365 (1984).

[54]A. Dovgal, V. Kozlov, and A. Michalke, Progress in Aerospace Sciences **30**, 61 (1994).

[55]L. E. Jones, Ph.D. thesis, University of Southampton (2008).

[56]L.-S. Huang and C.-M. Ho, Journal of Fluid Mechanics **210**, 475 (1990).

[57]M. Drela and H. Youngren, Xfoil 6.94 user guide (2001).

[58]X. Chen and R. Agarwal, Journal of Aircraft **49**, 622 (2012).

[59]D. Greenblatt and I. Wygnanski, Prog. Aerosp. Sci. **36**, 487 (2000).

[60]C.-M. Ho and L.-S. Huang, Journal of Fluid Mechanics **119**, 443 (1982).

[61]S. L. Prigent, O. Buxton, and P. J. Bruce, in 54th AIAA Aerospace Sciences Meeting (2016), p. 0852.